Continental Shelf Research 38 (2012) 63–78

Contents lists available at SciVerse ScienceDirect

Continental Shelf Research

journal homepage: www.elsevier.com/locate/csr

Research papers

Surface gravity wave effects on the upper ocean boundary layer: Modification of a one-dimensional vertical mixing model

Mostafa Bakhoday Paskyabi [a,*], Ilker Fer [a], Alastair D. Jenkins [b]

[a] Geophysical Institute, University of Bergen, Allégaten 70, 5007 Bergen, Norway
[b] Uni Computing/Bjerknes Centre for Climate Research, Geophysical Institute, Allégaten 70, 5007 Bergen, Norway

ARTICLE INFO

Article history:
Received 17 October 2011
Received in revised form
5 January 2012
Accepted 7 March 2012
Available online 16 March 2012

Keywords:
Surface gravity wave
Stokes drift
Ekman current
Turbulence closure
Vertical mixing
Wave energy spectrum

ABSTRACT

The impact of ocean surface gravity waves on the near-surface currents and on the upper ocean mixed layer is investigated using the one-dimensional general ocean turbulence model (GOTM). The goal of the investigation is to determine coupling methodology which required theories, modifications and parameterizations to incorporate the influence of surface wave forcing into an ocean dynamic model. To this end, some well-known theories of air–sea interaction are applied to modify momentum and energy equations to include the surface wave stress, wind energy input, wave dissipation, and Stokes drift. A two dimensional wave energy spectrum is used as a representative sea state for a sufficiently large fetch. The performance of the wave-modified model is tested by a series of model experiments which cover a number of features of the upper ocean boundary layer on diurnal and seasonal time scales. These sets of model experiments include both some idealized test cases to show the importance and sensitivity of the upper ocean to wave parameterizations, and some additional observation-oriented experiments which highlight the role of the modifications in improving the prediction of the upper ocean dynamical variability. The results confirm again the dominant role of Stokes drift in influencing both the magnitude and the angular turning of the surface Ekman current and the evolution of the upper ocean boundary layer (mixed layer depth and temperature evolution), in comparison with other wave induced parameters. Meanwhile, it is shown that the modified model is sensitive to wave parameterizations and the wave energy spectrum. However, there remain a number of uncertainties due to choice of wave energy spectrum, wave forcing parameterization, the surface eddy viscosity, momentum and energy surface boundary conditions, and the role of some important processes excluded from this study, such as the effect of Langmuir circulations.

1. Introduction

The air–sea interface sets the boundary conditions for physical and biogeochemical processes in the marine atmospheric planetary boundary layer and the upper ocean mixed layer (OML). The processes in this complex interface and the coupling between surface gravity waves, winds and currents in the adjacent turbulent boundary layers play a key role in the global climate system (Sullivan and McWilliams, 2010). Fluxes of momentum, heat and gases across this interface influence the weather and climate (McWilliams, 1996), and spatial distribution and evolution of greenhouse gases (Wanninkhof et al., 2009). In OML, the present state-of-the-art lacks a satisfactory description of the energetics of turbulence. This is largely due to challenges associated with acquiring accurate observations and conducting numerical simulations in a turbulent environment with a dynamic interface supporting surface gravity waves spanning wavelengths from millimeter to hundreds of meters. Non-linear processes over aerodynamically rough and wavy surface, intermittent wave breaking, generation of spray and bubbles further complicate the description and quantification of processes at play (Melville, 1996; Gemmrich, 2010; Terray et al., 1996; Gemmrich and Farmer, 2004; Sullivan and McWilliams, 2010).

The salient features of the air–sea interaction and its important role have been reported in theoretical (Jeffreys, 1925; Miles, 1957), observational (Snyder et al., 1981; Komen et al., 1984), and numerical (Wam, 1988; Tolman, 2002; Tolman and Chalikov, 1996) studies in the past several decades. McWilliams and Restrepo (1999) reported the substantial impact of Stokes transport on carrying the mechanical energy through the surface waves, as well as on the Ekman turning of surface current. Hasselmann (1970) demonstrated that in a rotating ocean, the wave induced Stokes drift, so-called Coriolis–Stokes forcing (Polton et al., 2005), influences the mean flow with a zero Lagrangian mean by a factor proportional to $f_{cor} \times U_s$,

* Corresponding author.
E-mail addresses: Mostafa.Bakhoday@gfi.uib.no (M. Bakhoday Paskyabi), ilker.fer@gfi.uib.no (I. Fer), Alastair.Jenkins@uni.no (A.D. Jenkins).

0278-4343/$ - see front matter © 2012 Elsevier Ltd. All rights reserved.
http://dx.doi.org/10.1016/j.csr.2012.03.002

where f_{cor} is Coriolis parameter and U_s is the Stokes drift (Jenkins, 1987; Andrews and McIntyre, 1978).

Waves not only extract energy from the wind, but also modify the effective momentum flux into current, and also influence the wind field. Longuet-Higgins (1953) investigated the effect of viscosity on damping of the wave in the absence of rotation. He showed that the presence of even small viscosity modifies strongly the momentum transfer in a thin boundary layer (vorticity layer). Weber (1983a,b) investigated the combination of Stokes drift with inertial oscillations and energy conversion from waves to currents in the presence of small eddy viscosity (see Jenkins, 1989 for general time-dependent forcing). Jenkins (1989) modified the classical Ekman problem by adding Coriolis–Stokes forcing and a term for redistributing the momentum lost from the waves by dissipation. He pointed out that the eddy viscosity which acts on the mean flow cannot be the same as that acting to damp out waves. Polton et al. (2005) followed the idea of Jenkins (1989) and solved the same problem analytically using a constant and a linearly varying eddy viscosity.

In addition to transfer of energy and momentum by the surface wave field, waves breaking or non-breaking enhance the near-surface turbulence (Kantha and Clayson, 2004; Kitaigorodskii et al., 1983). Observations by shipborne (Drennan et al., 1996), wave following (Soloviev and Lukas, 2003), and profiling instruments (Anis and Moum, 1995; Stips et al., 2005) in the past few years have confirmed that the breaking waves generate a source of turbulent kinetic energy (TKE) and enhance the dissipation rate of TKE, ϵ, to levels much greater than those of predicted by the classical law of the wall (LOW). Terray et al. (1996) obtained an almost universal relationship between dimensionless ϵ (scaled as a function of wind speed, wave phase speed, significant wave height and depth), and dimensionless depth (scaled by significant wave height). They divided the mixed layer into a wave breaking sublayer, a transition sublayer, and a LOW layer. The wave breaking sublayer is the layer with direct injection of TKE by breaking waves in which ϵ is nearly constant and the rate of shear production contribution in the TKE balance is assumed negligible. In the transition sublayer, the vertical transport of TKE enhances the shear production. ϵ scales with wind-wave parameters and decays with depth, $\epsilon \approx z^a$, with a log–log slope of $a = -2.3 \pm 0.4$ (Stips et al., 2005). In the deepest layer, ϵ obeys the LOW.

In recent years, a number of one-dimensional models have been applied to highlight the role of surface wave breaking and its effects on near-surface currents and turbulence. Craig and Banner (1994) employed an improved 2.5 level closure model by following the work of Mellor and Yamada (1982). They applied a new parameterization for the surface TKE flux as ηu_*^3, where η is referred to as wave energy parameter and is argued to be dependent on the wave age (Terray et al., 1996) and u_* is the friction velocity on the water-side. Based on best fit to observations, Craig and Banner (1994) obtained $\eta = 100$, and many other numerical models adapted this choice (Burchard and Bolding, 2001). Stips et al. (2005) measured small scale shear and temperature fluctuations using a rising microstructure profiler under very weak stratification and fetch-limited conditions. Based on observations and model simulations in the wave affected sublayer, they found that ϵ decays with depth with a slope between -2.1 and -1.7 in a log–log representation. Jones and Monismith (2007) measured the vertical distribution of TKE dissipation rate using an array of four acoustic Doppler velocimeters under a white-capping wave. They pointed out that without the incorporation of wave forcing (whitecapping effects), the numerical models will not predict the correct distribution of TKE and for 50% of the one-month length of their experiment the wave affected surface layer extended over 90% or more of the water column in the absence of stratification.

Due to importance of coupling the impact of wave field on the near-surface current and turbulence, several coupling experiments have been done in recent years. Perrie et al. (2003) used the theory of Jenkins (1989) and employed a simple diagnostic ocean model with an Ekman layer and depth independent eddy viscosity. Lewis and Belcher (2004) studied the surface Ekman current analytically and found a deflection of the surface current of between 10° and 45°, and a deflection of the sub-surface current by approximately 75° from the wind stress at a depth between 5 and 20 m, and rapid current attenuation with depth. Tang et al. (2007) applied the same methodology as Perrie et al. (2003) and computed the wave effect on the surface current using Jenkins (1989) by modifying the Princeton Ocean Model. Song and Huang (2011) and Song (2009) presented steady state analytic and approximate solutions for modified Ekman equations modified to take account of wave effects with different choices for eddy viscosity dependency. Sullivan et al. (2007) used stochastic breakers with a normalized probability distribution function for the random breaker impulses to study the interplay between breaking and vortex forces in the presence of breaking waves. By large eddy simulation, they verified the impact of stochastic breakers in the enhancement of the near-surface mixing. Pursuing Sullivan et al. (2007), stochastic breakers concept, He and Chen (2011) modified the momentum equations of GOTM in the presence of wave breaking using vertical distribution of wave breaking stress.

Besides the effect of wave breaking, the role of non-breaking waves for transferring of energy to the upper ocean mixing (so-called wave–turbulence interaction) has been investigated in several theoretical, experimental, and observational studies (Kitaigorodskii et al., 1983; Babanin and Haus, 2009; Ardhuin and Jenkins, 2006; Anis and Moum, 1995; Gemmrich and Farmer, 2004). Qiao et al. (2004) proposed a parameterization of non-breaking wave-induced mixing in circulation model formulated by the wavenumber spectrum. Dai et al. (2010) based on measuring the thermal destratification in a wave tank demonstrated that the mixing induced by non-breaking surface wave may have an important impact on the vertical mixing process. Furthermore, they suggested a way to parameterize wave-induced mixing in the numerical ocean models. Recently, Huang et al. (2011) applied wave–turbulence interaction to a one-dimensional model with Mellor–Yamada scheme. They pointed out that non-breaking wave influences on the upper ocean mixing extend to much greater depths than wave breaking, and that wave–turbulence interaction parameterization can improve efficiently the problem of insufficient mixing in the classical Mellor–Yamada model.

In this study, following Perrie et al. (2003) and Tang et al. (2007), theoretical and numerical procedures are described to achieve a coupled air–sea modelling system for evaluating the impact of the wave field on the near-surface currents and on the dynamics of the upper ocean mixed layer. The modelling in our study consists of calculating the atmospheric source terms introduced in the ocean surface gravity wave model (Komen et al., 1984; Janssen, 1991, 1989; Jenkins, 1992), and applying direct coupling of GOTM with wave forcing at each time step based on the theory of Jenkins (1986, 1987, 1989) in which upper ocean momentum and energy partial differential equations are modified by wave energy fluxes. The Donelan and Pierson directional wave spectrum (Donelan and Pierson, 1987) is used to calculate the Stokes drift, the wave induced momentum flux, and the energy flux for coupling purposes for a fully developed wind sea. This simple estimate of the wave energy spectrum cannot support many complex features of ocean wave variability, however, it provides a good framework for this study. A series of test cases to investigate the wave effects on the upper ocean boundary layer on the diurnal and seasonal time scale has been conducted to cover different features of wind–wave and wave–current interactions. The wave effects on the model simulations are introduced by switching on the wave forcing. Furthermore, a steady state wave modified Ekman current is included in the test cases for a depth dependent eddy viscosity. It is not the scope of this study to confirm the existence of wave effects because the details of ocean mixing response to wind and wave forcing are quite well established. The purpose is to document an comprehensive review of modifications of GOTM to incorporate wave induced fluxes and further to test the skill of the modified model by comparing the results to observations reported in the literature.

This paper is organized as follows. A brief description of modification components in the coupled modelling system is presented in Section 2. The source terms of wave energy balance equation that are used to estimate momentum and energy fluxes are described, and modifications of the GOTM governing equations in the presence of wave field fluxes are summarized. The effect of modifications are presented in Section 3 using numerical experiments and comparisons with observations. The final section presents a discussion and summary.

2. Coupled atmosphere and ocean

The interaction of wind, surface gravity waves and oceanic currents is an important factor for better estimation of the momentum and energy fluxes at the air–sea interface. Ocean surface gravity waves are an important manifestation of this air–sea interaction that can modify Stokes drift and turbulent mixing near the upper ocean boundary layer due to wave breaking. The impact of surface waves on the atmosphere also is linked into the wave stress (Section 2.1) which is dependent on wind–wave spectrum. The evolution of the wave spectrum is based on a spectral energy or action balance equation (Tolman and Chalikov, 1996). In deep ocean with no refraction and no significant current, the variance density spectrum $E(f,\theta)$ of the sea surface elevations takes the following radiative transfer equation form:

$$\frac{\partial E}{\partial t}+\nabla(c_g E)=S_{nl}+S_{in}+S_{ds}, \tag{1}$$

where the left hand side represents the evolution of the directional energy spectrum E as a function of frequency $f=\omega/2\pi$, and wave direction θ. Here S_{nl} is the non-linear wave-wave interaction term, S_{in} is the wind energy input into the wave field, S_{ds} is the wave dissipation due to whitecapping, breaking and bottom friction, c_g is the velocity of wave energy propagation (group velocity), and ω is the angular frequency.

Fig. 1 illustrates a typical wave energy spectrum with four energy flux regions based on three characteristic frequencies f_o, f_{eq} and f_{ds} (Resio and Long, 2004). At frequency f_o, the net energy flux due to nearly equal positive and negative front lobe of S_{nl} is zero and in this region only the wind energy input S_{in} gives gain in total energy. The second region is the transition region between the peak region and the equilibrium region (III) where energy is transported from low to higher frequencies. The final region is where all the energy received from regions II and III is lost by either wave breaking or viscosity.

The conservation properties of the non-linear energy transfer between wave components imply that S_{nl} integrates to zero over the whole frequency domain, so only S_{in} and S_{ds} contribute to the energy and momentum balance of the mean flow and turbulence. The approximate forms of S_{in} based on linear and exponential growth rate, and the S_{ds} function are discussed in Appendix A. In this section, a brief description is given of source terms in Eq. (1) and how they relate to the major coupling process of air–sea interaction such as wave-induced flux and wave–current interaction. The effects of these coupling processes in the GOTM governing equations are presented.

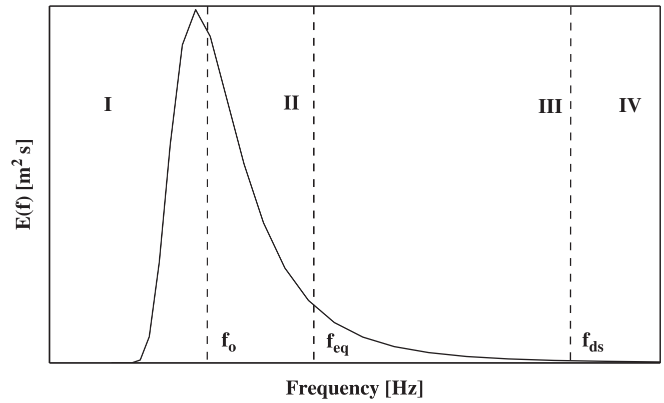

Fig. 1. Four energy flux regions in the wave energy spectrum $E(f)$.

2.1. Wave-induced flux

The total wind stress near the surface can be represented as

$$\tau_{tot}=\tau_{wave}+\tau_{turb}+\tau_{visc}, \tag{2}$$

where τ_{wave}, τ_{turb} and τ_{visc} are wave-induced stress, turbulent stress and viscous stress. The atmospheric turbulence flux decreases to zero at the surface where the turbulence vanishes. The total wind stress is therefore a result of the air–sea interaction as friction of airflow against water surface depends strongly on sea surface roughness length. In weak wind conditions, this roughness is small, and in strong cases especially in the presence of active wave breaking, the surface is aerodynamically rough (Tsagareli et al., 2010). The relation between this roughness and the magnitude of stress is determined by applying a drag coefficient that depends on relative motion between the air and the waves of different phase velocities. Waves which propagate with a phase velocity equal to or greater than those of the mean wind speed should make only a small contribution to the momentum flux into the ocean. The high-frequency gravity waves which move slower than the wind will make a larger contribution to the surface drag (Janssen, 1989).

The momentum flux, or stress, is related to the input source term in the wave energy balance equation (Jenkins, 1989)

$$\vec{\tau}_{wave}=2\pi\rho_w\int_f\int_\theta f\hat{\mathbf{k}}S_{in}(f,\theta)\,d\theta\,df, \tag{3}$$

here ρ_w is the water density, $\omega=2\pi f$, and $\mathbf{k}=\hat{\mathbf{k}}k$ is the horizontal wavenumber vector with modulus k and direction $\hat{\mathbf{k}}=(\cos\theta,\ \sin\theta)$. The wind energy input term, S_{in}, is determined by applying both a linear growth rate (Eq. (A.2)) (Snyder et al., 1981; Komen et al., 1984; Hasselmann et al., 1988) and an exponential growth rate (Eq. (A.3)) (Janssen, 1989). Resio and Long (2004) and Kudryavtsev and Makin (2002), based on observations and numerical studies, reported that more energy/momentum transfer occurs at frequencies above f_{eq} (up to 70%). Thus, the high frequency part of the wave energy spectrum and correspondingly the wind energy input source term, S_{in}, play a key role in calculation of stress/momentum transfer. As a constraint on the magnitude of the wave-induced stress obtained from Eq. (3), the following bulk relation

$$\tau^b_{wave}=\rho_a U^2_{10}(C_d-C_v) \tag{4}$$

is employed. Here $C_v=-5\times10^{-5}U_{10}+1.1\times10^{-3}$ is the viscous drag coefficient, U_{10} is the wind speed in m s^{-1} at the height of 10 m, ρ_a is the air density, and $C_d=[0.78+0.475f(\delta)U_{10}]\times10^{-3}$ is the wave age dependent drag coefficient, $f(\delta)=0.85^B A_G^{1/2}\delta^{-B}$,

$\delta = h_s\omega_p^2/g$ is the wave steepness, h_s is the significant wave height, ω_p is the wave angular frequency at the spectral peak frequency, and A_G=1.7 and $B=-1.7$ are the empirical parameters (Guan and Xie, 2004). Using the inequality

$$|\vec{\tau}_{wave}| \leq \tau^b_{wave}, \tag{5}$$

in which $|\cdot|$ denotes modulus of a vector, S_{in} can be calibrated. The wave stress (Eq. (3)) can be separated into two frequency components

$$\vec{\tau}_{wave} = \underbrace{2\pi\rho_w \int_{f\leq f_c}\int_\theta f\hat{\mathbf{k}}S_{in}\,d\theta\,df}_{\Lambda^1_{in}(f_c)} + \underbrace{2\pi\rho_w \int_{f>f_c}\int_\theta f\hat{\mathbf{k}}S_{in}\,d\theta\,df}_{\Lambda^2_{in}(f_c)}, \tag{6}$$

where f_c is a critical frequency. Following Tsagareli et al. (2010), f_c must be determined such that the first term on the right hand side of Eq. (6) is less than τ^b_{wave}. This frequency is a good criteria for separating the frequency range of the dominant growth rate of wave energy. Thus, it is possible to use f_c to reduce or increase the wind-input energy source term, depending on the magnitude of a correction factor X which satisfies $S^{corr}_{in}(f) = XS_{in}(f)$ and the constraint $|\Lambda^1_{in}|(f_c) \leq \tau^b_{wave}$. After this correction, it is assumed that there is a sharp contrast at frequency f_c. The physical effects of a discontinuous jump can be reproduced by applying a smooth and continuous function $L(X)$ such that $S^{corr}_{in}(f) = L(X)S_{in}(f)$. For more details, the reader is referred to Tsagareli et al. (2010).

Note that to compute the above frequency integrals for frequencies greater than the operational frequency, f_{max}, of the measuring instrument, a power law is applied. The pioneering work for this power law assumption originated from Phillips (1958) who proposed, based on dimensional arguments, that the shape of spectral density for frequencies above f_{eq} in the third region of Fig. 1 is independent of fetch, duration, and wind strength, and decays as f^{-5} with the wave frequency f. However, later observational studies confirmed a frequency dependency closer to f^{-4} for the frequencies above three times the peak frequency. Several studies support a power law in the range of -5 to -3.3 for the high frequency dependence of spectral density (Jones and Toba, 2008).

In this study, the two-dimensional Donelan–Pierson spectrum is used for generating wave energy spectrum for frequency range $f \leq f_{max}$ (Appendix D) and the spectrum for frequencies $f > f_{max}$ is assumed to be proportional to f^{-5}, and the wave spectrum is approximated by $E(f,\theta) = (f/f_{max})^{-5}E(f_{max},\theta)$.

2.2. Wave–current interaction

The shear in the wave-induced Stokes drift velocity extracts energy from surface waves and injects it into the near-surface turbulence (Jenkins, 1989). The Stokes drift for deep water is

$$\mathbf{U}_s(z) = 4\pi \int_\theta \int_f f\mathbf{k}E(f,\theta)e^{-2k|z|}\,df\,d\theta, \tag{7}$$

where $\mathbf{k}$ is the wavenumber vector (Huang, 1971). The contribution to the Stokes drift is maximal in the peak region of the wave spectrum. Meanwhile, near the surface, short waves give a significant contribution to $\mathbf{U}_s$ (Polton et al., 2005; Tang et al., 2007). In order to include the effect of Stokes drift on current as well as the wave-induced momentum transfer from waves to ocean due to dissipation of wave energy, the governing momentum equations in GOTM are modified by including the Stokes drift in the Coriolis term and another momentum source term, $\mathbf{F}_{ds}$ as

$$\dot{\mathbf{U}} = \mathcal{D}_\mathbf{U} - g\nabla_h\zeta + \int_z^\zeta \nabla_h B\,dz' - f_{cor} \times (\mathbf{U}+\mathbf{U}_s) + \mathbf{F}_{ds}, \tag{8}$$

where $\dot{\mathbf{U}}$ denotes the total derivative of vector $\mathbf{U}$, ζ the free surface elevation, ∇_h the horizontal gradient operator, and B the mean buoyancy. $\mathcal{D}_\mathbf{U}$ is the sum of the turbulent and viscous transport term modelled according to

$$\mathcal{D}_\mathbf{U} = \frac{\partial}{\partial z}\left((\nu_t+\nu)\frac{\partial \mathbf{U}}{\partial z} - \tilde{\Gamma}_\mathbf{U}\right). \tag{9}$$

In this equation, ν_t and ν are the turbulent and molecular diffusivities of momentum, respectively, and $\tilde{\Gamma}_U$ denotes the non-local flux of momentum. The momentum source term $\mathbf{F}_{ds}$ due to the surface wave energy dissipation is defined as (Jenkins, 1987, 1989)

$$\mathbf{F}_{ds} = -4\pi \int_f \int_\theta fS_{ds}(f,\theta)\hat{\mathbf{k}}ke^{-2k|z|}\,d\theta\,df, \tag{10}$$

where z is the vertical distance from the mean water surface and $\hat{\mathbf{k}}$ is the unit vector in the direction of wave propagation. In Eq. (10), it is assumed that the transfer of momentum from wave to mean flow has exponential decay away from the surface by a vertical distribution $\exp(-2k|z|)$. In addition to above modification of momentum equation, Stokes drift is the driving parameter for Langmuir circulations that can be included by adding a vortex term $\mathbf{U}_s \times (\nabla \times \mathbf{U})$ on the governing momentum equations (Moon, 2005).

To estimate the effect of waves on the upper momentum boundary condition, the theory of Janssen (1991) is employed. By dividing both sides of Eq. (1) by the phase velocity and integrating, the equation of conservation of momentum is obtained. By substituting this differential equation into two-dimensional depth-averaged mass equations (Mastenbroek et al., 1993), the surface stress is obtained as

$$\vec{\tau}^{surf} = \tau_{tot} - 2\pi\rho_w \int_f \int_\theta \hat{\mathbf{k}}f(S_{in}(f,\theta)+S_{ds}(f,\theta)+S_{nl}(f,\theta))\,d\theta\,df.$$

The first term on the right-hand-side represents the momentum input from the wind. Part of this momentum goes into the waves instead of the current via the first term of the integrand (the wave induced stress, τ_{wave}). The second term in the integrand specifies the wave momentum which is transferred from the waves to the current at surface as a result of wave dissipation. Here, this term must be removed from boundary condition, since, the releasing of momentum due to dissipation of wave energy has been applied in the Eulerian mean current by the term $\mathbf{F}_{ds}$. Because the non-linear source term redistributes momentum and energy between different wave components, its integral over all wave components is zero. Thus, by ignoring the non-linear interaction effects, the reduced wind stress due to wave effects is employed as an upper boundary condition for the momentum equation

$$\rho_w \nu_t \frac{\partial \mathbf{U}}{\partial z} = \vec{\tau}^{surf}_{mod}, \tag{11}$$

where the modified surface stress is given by

$$\vec{\tau}^{surf}_{mod} = \tau_{tot} - 2\pi\rho_w \int_f \int_\theta \hat{\mathbf{k}}fS_{in}(f,\theta)\,d\theta\,df. \tag{12}$$

From Eq. (11), it can be seen that in the presence of waves there is a reduction in the current speed. However, this reduction can be compensated partially by the term $\mathbf{F}_{ds}$ in Eq. (10), i.e. the momentum flux into the water column that increases the near-surface current speed (Tang et al., 2007).

2.3. Wave effect and turbulence closure

The first attempt to model numerically the wave-enhanced turbulence in the near-surface layer was performed by Craig and Banner (1994). They employed the level 2.5 turbulence closure scheme of Mellor and Yamada (1982) with a simple model of the oceanic boundary layer to predict the enhanced near-surface turbulence (in the presence of wave breaking) in comparison with the standard LOW. By assuming that the production and dissipation rate of TKE are equal, the influence of wave breaking was modelled by including TKE injection as the surface boundary condition for the TKE differential equation. Burchard and Bolding (2001) employed a shear dependent closure based on a $k-\epsilon$ model for simulating the effect of wave breaking near the surface. The common technique for these models is the parameterization of the surface flux of TKE as a source for applying the effect of wave breaking to the numerical model. The surface TKE flux and the wind energy flux are assumed equal ($F_k \simeq \eta u_*^3$, and u_* is the water-side friction velocity). Various values have been proposed for η, such as $\eta = 80$ by Wang and Huang (2004), $\eta = 250$ by Feddersen and Trowbridge (2005), $\eta = 168$ by Gerbi et al. (2009) and so on. Terray et al. (1996), Mellor and Blumberg (2004) and Moon (2005) have used the following boundary condition for the TKE and the mixing length:

$$q^2(0) = (15.8\eta)^{2/3} u_*^2, \tag{13}$$

$$l(0) = \max[\kappa z_0, l_0], \tag{14}$$

where $q^2/2$ is the TKE, κ is the von Kármán constant, z_0 is a surface roughness length, u_* is the water-side friction velocity, l is the mixing length, and η is determined by

$$\eta = \frac{F_k}{u_*^3}. \tag{15}$$

The rate of wind energy input, F_k, to the waves from the winds is determined by integration of S_{in} in the whole frequency and direction range

$$F_k = g \int_f \int_\theta S_{in}(f,\theta)\, d\theta\, df, \tag{16}$$

where $S_{in}(f,\theta)$ is defined by Eq. (A.1) based on the growth rate of Eq. (A.4) (Moon, 2005). However, instead of relating the surface TKE flux to the wind stress ($\approx u_*^3$) or wind energy input (Eq. (16)), the transfer of kinetic and potential energy to enhance the near-surface TKE can be specified directly by the use of wave energy dissipation in the surface zone as

$$F_k = g \int_f \int_\theta S_{ds}(f,\theta)\, d\theta\, df. \tag{17}$$

Thus, the balance of vertical energy flux and TKE from breaking waves in the surface boundary condition (here Neuman (flux) boundary condition) can be written, for example, in the $k-\epsilon$ model as

$$\frac{\nu_t}{\sigma_k}\frac{\partial k}{\partial z} = -F_k, \tag{18}$$

where σ_k is the turbulent Schmidt number (Burchard and Baumert, 1995). For the lower boundary condition at the sea bottom, the zero flux of turbulent energy is assumed.

3. Results and discussion

Surface wave stress is calculated based on both linear ($\tau_{wave}^{H,notail}$ without and $\tau_{wave}^{H,tail}$ with the tail effect) and exponential growth rate ($\tau_{wave}^{J,notail}$ without and $\tau_{wave}^{J,tail}$ with tail and correction effect). The wave stress based on the exponential growth rate introduced in Eq. (A.3) is prescribed iteratively following the algorithm described in Appendix B. The wave stress together with the x-component of Stokes drift at the surface, $u_s(z_{surf})$, is presented in Table 1 for wind speeds ranging from 5 to 30 m s^{-1} for five realizations. Hereafter, the tail effect and wave-induced momentum correction mechanism are imposed into the calculation of wave stresses. Thus, the expressions τ_{wave}^{J} and τ_{wave}^{H} denote the wave stresses including the tail effect and correction algorithm for exponential growth rate, and the tail effect for the linear growth rate, respectively. To include shortest waves in the capillary wave range, the f_∞ is set to 10 Hz. Furthermore, the frequency domain $[f_{min}, f_{max}]$ is defined by the interval [0.05,0.5]. According to Table 1, for a wind speed of 5 m s^{-1} the wave stress contribution τ_{wave}^{b} to the total surface stress τ_{tot} is about 6% and this contribution grows with increasing wind speed. The first row in Table 1 shows the inverse wave age, U_{10}/c_p, where c_p is the wave phase speed at the peak frequency of the wave energy spectrum. In the classical wave age scaling, a wave spectrum is defined as a young developing sea if its inverse wave age exceeds unity. The young sea will reach fully developed state for the inverse wave age in the range of 0.8–1.0. Energy input from wind ceases when the wave phase speed exceeds the wind speed ($U_{10}/c_p < 1$). In this case, the fully developed sea gradually dies out and the wave energy spectrum is considered old. In our setup, this parameter presents a fully developed sea.

Table 1
Applied x-component of wave stresses, N m^{-2}, and Stokes drift u_s, m s^{-1}, for different wind speeds, U_{10}, m s^{-1}. $\tau_{tot}^{J,notail}$ and $\tau_{tot}^{J,tail}$ are the total surface stress using iterative technique for exponential growth rate without and with tail and correction influences, $\tau_{wave}^{H,notail}$ and $\tau_{wave}^{H,tail}$ are wave stresses based on linear growth rate without and with tail effect, $\tau_{wave}^{J,notail}$ and $\tau_{wave}^{J,tail}$ are wave stresses based on exponential growth rate without and with tail and correction effects, and τ_{wave}^{b} is the wave stress based on bulk formula (Eq. (4)).

U_{10} (m s^{-1})	5	10	15	20	25	30
U_{10}/c_p	0.832	0.833	0.835	0.862	0.934	1.043
τ_{tot}	0.034	0.174	0.479	1.008	1.819	2.970
$\tau_{wave}^{H,notail}$	0.006	0.038	0.117	0.267	0.506	0.854
$\tau_{wave}^{H,tail}$	0.016	0.094	0.274	0.601	1.124	1.895
$\tau_{tot}^{J,notail}$	0.039	0.177	0.487	1.025	1.849	3.019
$\tau_{tot}^{J,tail}$	0.031	0.165	0.450	0.933	1.668	2.715
$\tau_{wave}^{J,notail}$	0.009	0.043	0.128	0.2916	0.585	1.071
$\tau_{wave}^{J,tail}$	0.005	0.081	0.331	0.7470	1.368	1.899
τ_{wave}^{b}	0.006	0.087	0.241	0.794	1.395	2.111
$u_s(z_{surf})$	0.059	0.118	0.178	0.237	0.296	0.356

In order to test the efficiency and performance of the wave-modified one-dimensional mixing model, some test cases are constructed. These cover the response of the near-surface current profile to waves and the wave effect on upper ocean mixing on diurnal and seasonal time scale, and are based on a set of idealized experiments and observation-oriented simulations. In the first part of this investigation, the effect of waves on a classical Ekman current is studied by numerical solutions of a simple Galerkin Finite Element Method (GFEM) (Appendix C). Solutions including wave are compared to those without wave effects. The mean field is specified as fully developed wind generated sea, and the eddy viscosity profiles are assumed depth-dependent but time invariant. In addition, to test the applicability of including wave effects in the real ocean, some comparisons are made using well-known published observational data. Furthermore, to check the accuracy of GFEM simulations, an analytical solution of the near surface wave-modified Ekman equations is given in Appendix E for depth-independent eddy viscosity. In the second part of this section, the modified GOTM model is applied to study various features of wave effects on the oceanic boundary layer on diurnal and seasonal time scales.

3.1. Wave effect on Ekman current: idealized case

To show the physical behavior of wave forcing, the stationary solutions of Eq. (8) are studied using both constant and linearly increasing eddy viscosity profiles. To provide external wave forcing such as wave momentum flux, energy flux, and Stokes

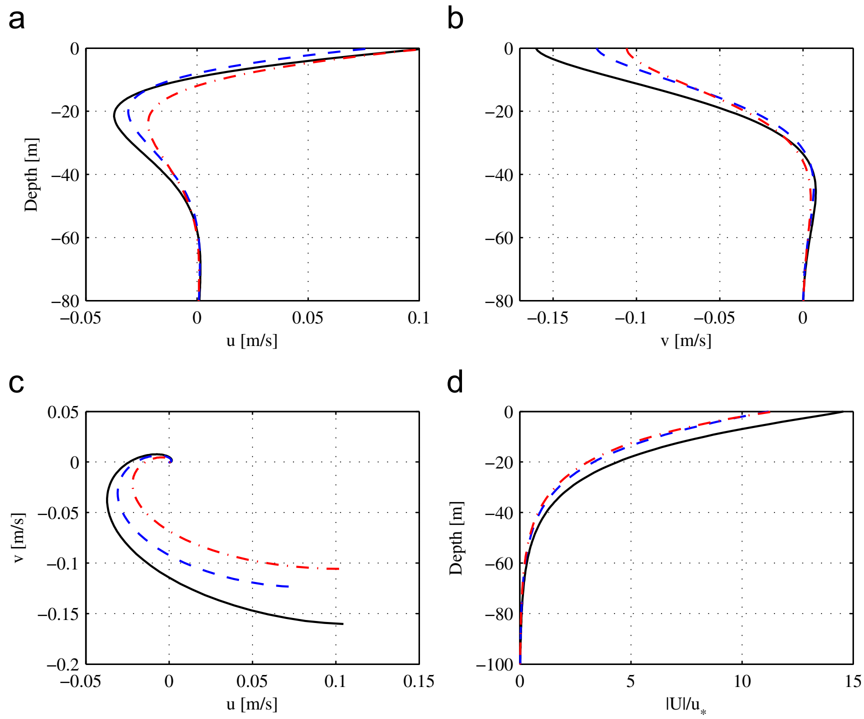

Fig. 2. Comparison of the vertical current profile for full wave forcing impact (solid lines), wave forcing in the absence of Stokes drift effect (dashed lines), and the classical Ekman solution (dash-dotted lines) for wind speed $U_{10}=10\ \mathrm{m\,s^{-1}}$ in the upper 100 m of the water column. (a and b) u and v components of vertical current vector for different wave forcing cases, (c) depth-dependent hodograph of the current for the different wave forcing cases, and (d) profiles of speed modulus, $|U|=\sqrt{u^2+v^2}$, normalized by the water-side friction velocity u_*.

drift, the wave spectrum is approximated by the Donelan and Pierson (DP) spectrum (Donelan and Pierson, 1987) (Appendix D) which corresponds to a fully developed sea state. In simple form, assuming negligible pressure gradient and horizontal homogeneity, Eq. (8) can be written in complex notation as

$$\frac{\partial}{\partial z}\left(\nu_t\frac{\partial \mathbf{U}}{\partial z}\right)=if_{cor}(\mathbf{U}+\mathbf{U}_s)+\mathbf{F}_{ds}, \tag{19}$$

where $\mathbf{U}=u+iv$ is the quasi-Eulerian current, $\mathbf{U}_s=u_s+iv_s$ is the Stokes drift, $\mathbf{F}_{ds}=f^x_{ds}+if^y_{ds}$ is the wave induced momentum transfer from waves to the ocean due to wave energy dissipation, and $i=\sqrt{-1}$. The upper boundary condition is given by Eq. (11). For the lower boundary condition, it is assumed $U\to 0$ as $z\to-\infty$.

A simple GFEM is applied to solve Eq. (19) numerically (for more details see Appendix C). In Fig. 2, the GFEM solutions of wave-modified Ekman current (Eq. (19)) are shown for the case of constant eddy viscosity $\nu_t=1.2\times10^{-4}\ \mathrm{m^2\,s^{-1}}$, $\rho_w=1025\ \mathrm{kg\,m^{-3}}$, $\rho_a=1.22\ \mathrm{kg\,m^{-3}}$, $U_{10}=10\ \mathrm{m\,s^{-1}}$. The Ekman layer depth is h_e=15.5 m. The wind stress and the wave directions are along the positive x-axis. Fig. 2a, b, d shows the vertical profiles of velocities. Despite large current shear in the upper few metres, below 60 m both the angular turning (Fig. 2c) and the velocity components approach zero. In comparison with the classical Ekman solution, the momentum reduction in the presence of wind energy input source term and wave dissipation source term, in the absence of Stokes drift, has a small but discernible contribution in modifying the surface current velocities, and increases the angular turning from 45° to 45.8° (Fig. 2c). However, when the Stokes drift is included the angular turning increases from 45° to 56° and the surface current magnitude increases by more than 35% (see also Jenkins, 1987; Weber, 1983b; Lewis and Belcher, 2004; Polton et al., 2005; Song, 2009; Tang et al., 2007). In fact, this example shows that the Stokes drift vertical distribution with the attenuation scale of inverse of the dominant wavenumber can influence almost the entire Ekman layer.

Fig. 3 illustrates the behavior of surface wave-modified Ekman current as a function of wave stress (linear growth rate τ^H_{wave} and exponential growth rate τ^J_{wave}). The impact of the wave dynamic source term parameterization (and also the wave energy dissipation parameterization) should not be ignored in the wave-induced momentum transfer.

3.2. Wave effect on Ekman current: observational case

Two sets of observations are used to compare the results of the GFEM with observations similar to those reported by Price and Sundermeyer (1999). These data sets were extracted directly from the figures in Price and Sundermeyer (1999) and thus they are not accurate. These data sets are the Long Term Upper Ocean Study (LOTUS3) and the Eastern Boundary Current (EBC) experiment. The LOTUS3 data were acquired during summer at 35°N in the Sargasso Sea with the average wind stress $\tau_{tot}=0.07$ Pa, and the average wind speed 6.8 m $\mathrm{s^{-1}}$. The reference depth H_G for this data set at which current can be assumed to be purely geostrophic is about 50 m (Lewis and Belcher, 2004). The EBC data were acquired at 37°N in the eastern North Pacific during the summer with average wind forcing $\tau_{tot}=0.09$ Pa, average wind speed 7.6 m $\mathrm{s^{-1}}$, and $H_G\approx 60$ m. For each of the two data sets, three runs are performed using the DP wave spectrum: runs with full wave forcing; wave impact without the Stokes drift effect; and no wave forcing. The GFEM results are shown in Fig. 4 together with the observations. In the GFEM runs, a linearly increasing eddy viscosity profile is used as suggested by Lewis and Belcher (2004) and Jenkins (1987)

$$\nu_t(z)=-\kappa u_*(z-z_0), \tag{20}$$

here z_0 is prescribed from an empirical model proposed by Mellor and Blumberg (2004). Following Terray et al. (1996) and Rascle

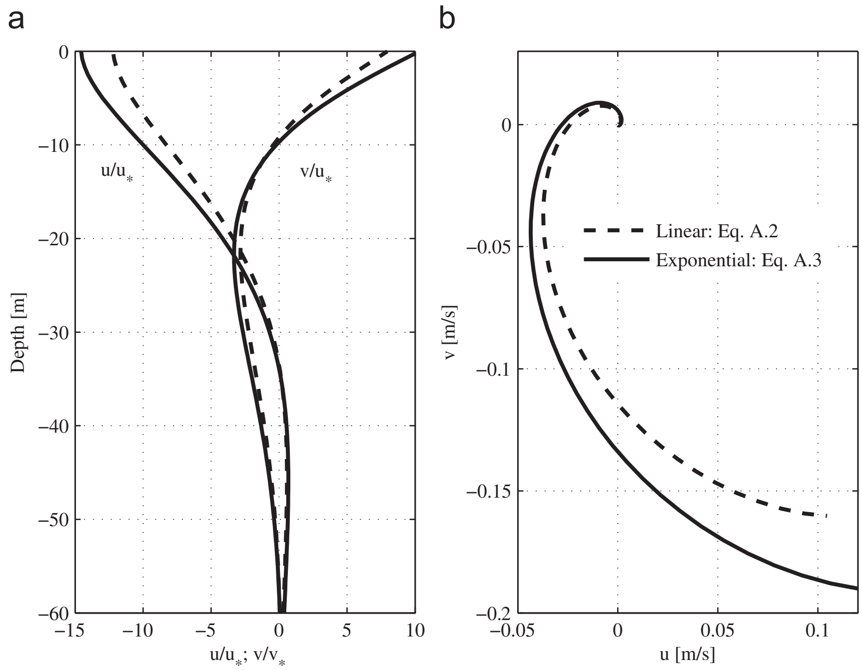

Fig. 3. Sensitivity of the calculated wave modified Ekman current to the wave dynamic source term parameterization S_{in} extracted from the growth rate of Eq. (A.2) (dashed lines) and Eq. (A.3) (solid lines).

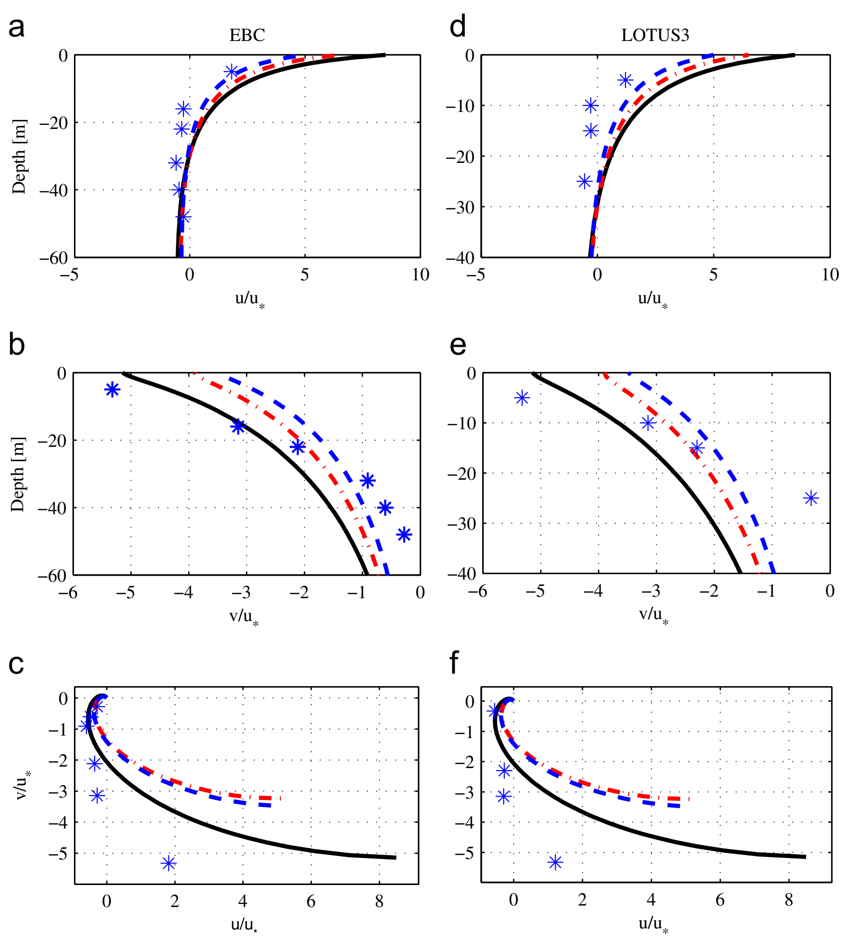

Fig. 4. Comparison of the GFEM results with linearly increasing eddy viscosity (Eq. (20)) with observed data from EBC (left column) and LOTUS3 (right column). The solid lines are profiles of runs with full wave effect, the dashed lines are profiles of runs excluding only the Stokes drift, and the dash-dotted lines show the results from runs without wave forcing. The observations (stars) are at −5, −15, −24, −32, −40, and −48 m for EBC data, and at −5, −10, −15, and −25 m for LOTUS3. The top and middle plots show the vertical profiles of downwind and crosswind velocity and the bottom plot shows the downwind velocity plotted against the crosswind velocity. All velocities are normalized by the water-side friction velocity u_*.

et al. (2007), it can be written

$$z_0 = 665\left(\frac{c_p}{u_*^a}\right)^{1.5}\frac{u_*^2}{g},$$

in which c_p is the phase velocity at the spectral peak frequency and u_*^a is the air-side friction velocity defined by Eq. (A.8). However, for a realistic comparison between simulated and observed results, in addition to surface wind stress, the effect of several other factors must be taken into account, including density stratification, buoyancy flux, heat flux, horizontal advection, and low frequency measurement errors in the near-surface boundary layer induced by wave-related motion of current meters attached to a surface buoy (Pollard, 1973).

For this experiment, the wave dissipation due to breaking does not have a significant impact in the water column, and wind energy input effect is also negligible compared with markedly improved estimation by Stokes drift effect. For run without wave forcing effect, the angular turning is about 40° for both the EBC and LOTUS3 cases. By introducing wave forcing, angular turning increases to 67° and 69°, respectively. Thus, the comparisons suggest that the veering in the surface layer down to about half of H_G is better captured when the wave forcing is included (see also Saetra et al., 2007).

The wave-modified solution is slightly sensitive to the choice of wind energy input parameterizations. Fig. 5 compares the velocity profiles for the two wind energy input parameterizations for the EBC case (solid lines use S_{in} defined by Eq. (A.3) and dashed lines use S_{in} defined from Eq. (A.2)).

3.3. Modified GOTM results with wave forcing

Validation of the modified GOTM is carried out by using idealized cases to check the model results for the response of the mixed layer depth and upper ocean dissipation rate of TKE to wind and surface gravity wave forcing. Three test cases based on observed data sets are constructed. The first observed profiles of temperature, salinity, and current are used as initial values for corresponding variables in GOTM. The GOTM relaxation scheme as a force for the prescribed profiles is switched off. The $k-\epsilon$ model is used to study one-dimensional mixing including a single partial differential equation for k, and a conservation differential equation for ϵ. The Neumann (flux) surface boundary condition is modified in k-equation (Eq. (18)) by including breaking wave effect. The Schumann and Gerz (1995) model is used to calculate the stability function of the $k-\epsilon$ model, and the minimum values are set for initializing the TKE and its dissipation rate. Numerical discretization is performed with a time step of $\Delta t = 60$ s and a vertical non-equidistance resolution with a slight zooming to the surface.

The DP directional wave spectrum is employed to estimate the characteristics of wind sea, wind energy source terms, wave stress, and the Stokes drift (Appendix D). The expression for S_{in} is from Janssen (1991) based on quasi-linear theory (Eq. (A.3)). The expression of Hasselmann (1974) is applied for the dissipation source term, S_{ds} (Eq. (A.7)).

3.3.1. Idealized case: wave-induced mixing

A simple idealized experiment is carried out using GOTM to predict the effect of wind and waves in the upper ocean mixed layer depth, and in the turbulent dissipation rate. In this idealized scenario, the latitude is 63.4°, water depth is 200 m, the temperature is 20 °C at surface and decreases by 0.005 °C m^{-1}. A constant wind stress of 0.2 N m^{-2} and upward heat flux of -100 W m^{-2} are applied to an ocean at rest (see also He and Chen, 2011). With this wind stress, we apply a corresponding fully developed sea based on the DP spectrum and obtain wave forcing factors: wind energy input source terms; Stokes drift; dissipation source term; and vertical momentum redistribution term calculated from the atmospheric conditions and the wave spectrum. To visualize the ocean mixed layer response to the forcing, we calculated the mixed layer depth (MLD) defined as the depth at which the density averaged in the upper 5 m increased to 20% of the difference between 100 m and the surface value. This is a robust estimate and is not influenced by the seasonal variation of the density jump at the base of mixed layer (Shaw et al., 2009). The distribution of the MLD for the first 9 days into

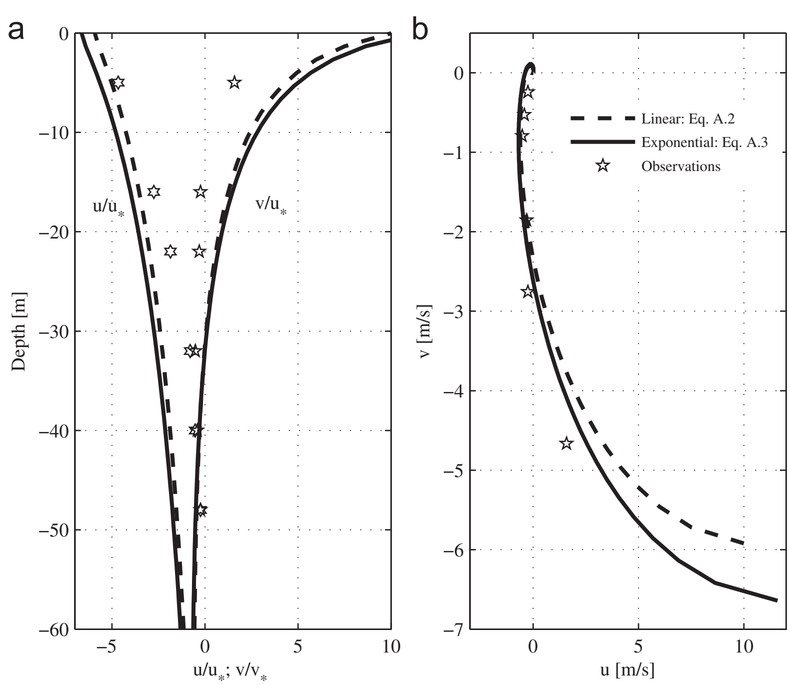

Fig. 5. Effect of different wave stress parameterizations for the EBC case. (a) Normalized velocity profiles and (b) angular turning of current. Solid lines are for exponential growth rate and dashed lines for linear growth rate. Observations are denoted by stars and hexagrams.

the simulation is shown in Fig. 6a. When the wave forcing is included in GOTM, the deepening of MLD is more pronounced. By day 9, MLD is about 48 m for no-wave and about 53 m with wave simulation. Corresponding rate of deepening of MLD, i.e. the entrainment velocity, is 2 m day^{-1} for no-wave and 2.4 m day^{-1} with wave effect, i.e. 20% larger.

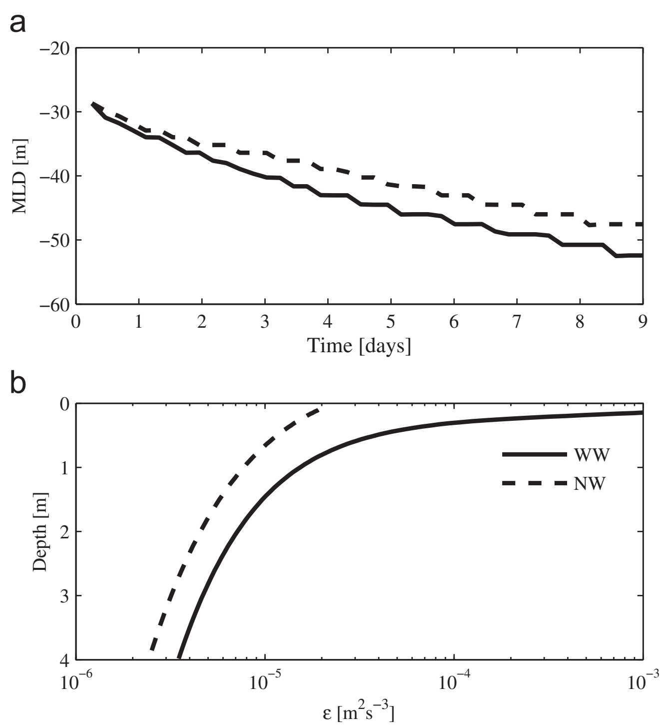

Fig. 6. Impact of waves on the development of the upper ocean mixed layer. (a) The MLD with wave forcing (WW) and no wave forcing (NW). The initial temperature profile decreases linearly by 0.005 °C m^{-1} from temperature of 20 °C at the surface. (b) The upper 5 m time-averaged profile of dissipation rate for the WW (solid lines) and NW (dashed lines) cases.

The time averaged profile of the modelled TKE dissipation rate is presented in Fig. 6b with and without wave forcing. In the wave forcing run, more TKE is injected in the upper few meters in comparison with the no-wave case. Averaged in the uppermost 1 m (43 grid points) $\epsilon = 3.0 \times 10^{-4}$ and 1.3×10^{-5} W kg^{-1} for with and without wave runs, respectively. A least-squares fit to an exponential decrease of the form $\epsilon \approx z^a$ reveals more details about deviation of the logarithmic slope a from the LOW criteria. The model output in no-wave case resembles typical slope between -1 and -0.2 in the uppermost 4 m, whereas if we include wave forcing this slope varies between -2.0 and -1 (Fig. 7a). The modelled results of this idealized scenario are compared to observations in the wave-affected surface layer reported by Stips et al. (2005). For this comparison, the depth is scaled by the significant wave height H_s (here 1.6 m extracted from the full spectrum) so that $\tilde{z} = z/H_s$, and the non-dimensional dissipation rate of TKE, $\tilde{\epsilon}$, is defined as $\tilde{\epsilon} = \epsilon H_s/F_k$ in which F_k is defined by Eq. (15). Fig. 7b shows that the dissipation rates follow the scaling of Terray et al. (1996) in good agreement with observations made by Stips et al. (2005) for run 2 (especially for $\tilde{z} \geq -1$) and Gerbi et al. (2009) for the significant wave height derived from full wave energy spectrum. The choice of significant wave height parameterization is important in scaling of depth and ϵ. Gerbi et al. (2009) pointed out that the H_s used in the Terray et al. (1996) scaling must be that of the wind waves, rather than that of the full spectrum.

3.3.2. Case study: Ekman current

A second test case is run in GOTM to study the response of near-surface current profiles to wind and surface gravity waves ignoring density stratification and buoyancy flux effects. In this run, the model is run for a period of one month forced with an average wind

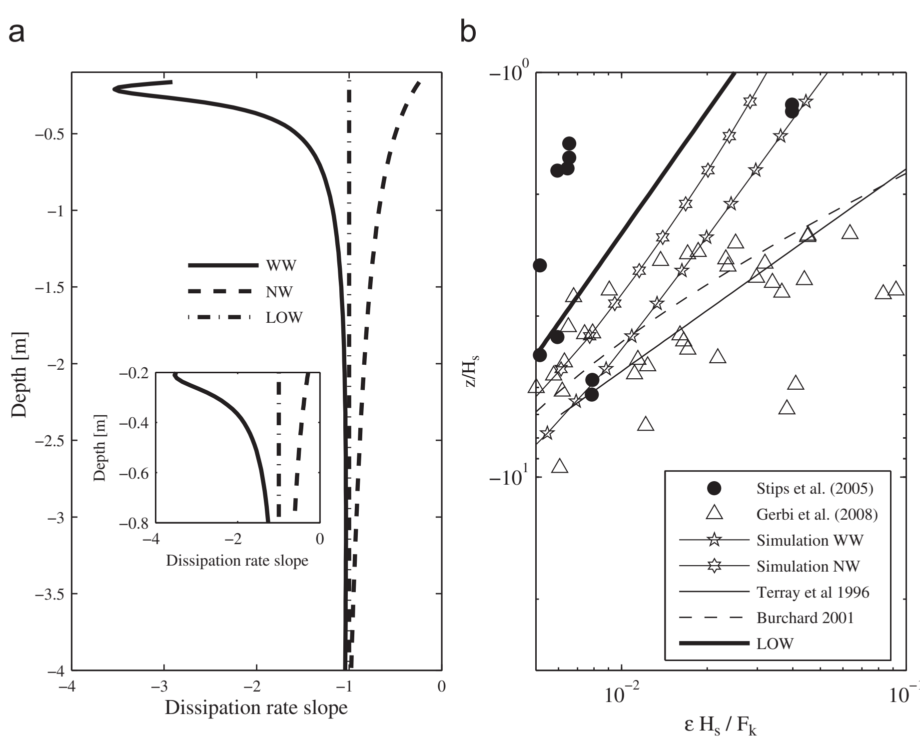

Fig. 7. (a) Profile of the exponential decay rate a of ϵ from fits of the form $\epsilon \propto z^a$ in the upper 4 m. The solid lines show the modified model result (WW), the dash-dotted lines show the standard law of the wall (LOW), and the dashed line shows model results without wave forcing (NW). The inset shows the profile of ϵ in the upper 0.8 m, (b) dissipation rates, normalized as suggested by Terray et al. (1996). The thick line is the dissipation rates using LOW, the thin line shows the scaling of Terray et al. (1996), and the dashed line shows the model prediction of Burchard and Bolding (2001) and Craig (1996).

speed $U_{10} = 6.8$ m s^{-1} and an average surface stress $\tau_{tot} = 0.07$ Pa. This forcing represents the average condition during LOTUS3 whereas it is about 10% weaker than EBC (Section 3.2). The wave field is assumed to be fully developed and the DP wave spectrum is applied to model the wave parameters (Appendix D). Fig. 8 presents the comparison among the GOTM simulation results (solid lines with wave forcing and dashed lines without wave effect), the GFEM steady state solution obtained by linearly increasing eddy viscosity (dash-dotted lines) (Appendix C), and LOTUS3 and EBC measured data sets (marked by stars) by including the Stokes drift effect. The model results exhibit good agreement with the measured current magnitudes and turning angle. However, there is little vertical shear and a flatness in observed vertical shear that does not describe accurately by the GOTM results. The discrepancy between the measurements and the numerical results may be explained by the effects of neglected heat flux and density stratification, the idealized sea state, uncertainties in the surface momentum and energy boundary conditions in the presence of breaking waves, and errors originated from current measurement due to sensor motion in the presence of wave motions. Rascle et al. (2007) constructed more realistic comparisons by including stratification and applying WAVEWATCH III (WW3) (Tolman, 2002) code to produce sea state with 1° resolution.

3.3.3. Case study: the northern North Sea

To check the ability of the wave-modified GOTM to model more realistic simulations, we applied the model to the data set from PROVESS experiment in the northern North Sea. The site is located at 59.3°N and 1°E and the water depth is 110 m. A 20-day period between 7 and 27 October 1966 is chosen and analysis of the whole water column for this period is confined only to dynamics of the surface mixed layer. The atmospheric forcing, wind stress and heat flux strongly increase after the first 7 days (Fig. 9a and c). The upper ocean response to this strong atmospheric forcing is severe erosion of the thermocline and also cooling of upper boundary layer by several degrees (Fig. 10a). The simulated temperature structure in the absence of waves shows weak near-surface temperature gradients, and the thermocline erosion and surface cooling are underestimated (Fig. 10b). When wave forcing is included, due to vertical fluxes imposed by the wave activities into the inertial motions, the agreement between observation and modified GOTM results (Fig. 10c) is satisfactory and gives a better estimate of mixing in comparison with the no-wave case. Thus, the vertical distribution of wave energy into the water column influences the mixing. The discrepancy in vertical mixing in the model and the observations may be a result of unresolved processes such as internal waves, or Langmuir

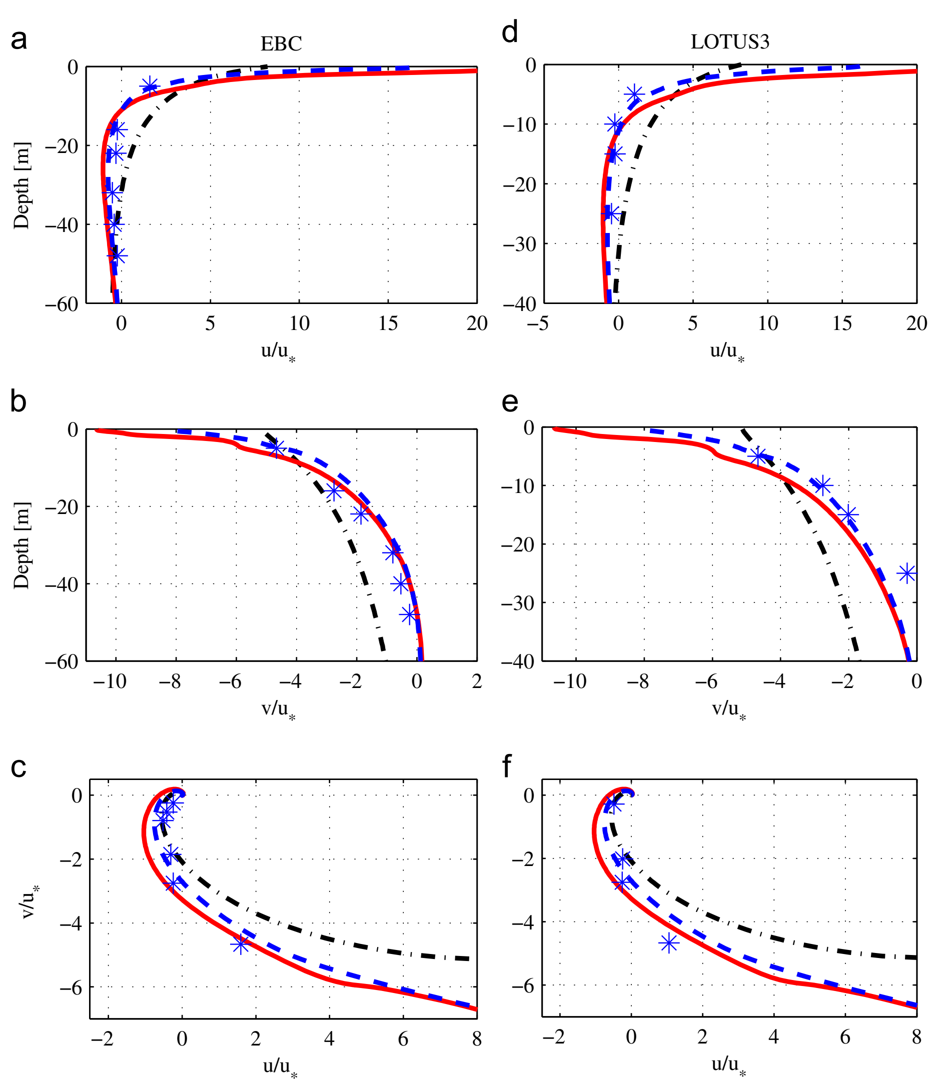

Fig. 8. Runs of GOTM with and without wave forcing and comparisons with the EBC (left) and LOTUS3 (right) denoted by stars. The dashed lines are GOTM runs without wave forcing effects and the solid lines are with wave effects. The dash-dotted lines present the GFEM results in the presence of wave influence. All velocities are scaled by the water-side friction velocity.

circulations, a non-realistic sea state, and uncertainties in the wave parameterizations.

3.3.4. Case study: Ocean Weather Station Papa

Ocean Weather Station (OWS) Papa long term observations of meteorological parameters and temperature profiles (at 50°N, 145°W) are applied as a final validation test case for the year 1966. OWS Papa is located in a region of the Pacific Ocean where the horizontal advection of heat and salt should be small (Burchard and Bolding, 2001), lending confidence on the use of a realistic one-dimensional oceanic model test case. The annual cycles of surface momentum flux and heat flux during the period of interest are plotted in Fig. 9b and d. The momentum flux is employed to extract ideal sea state parameters based on the fully developed DP wave spectrum (Appendix D). Fig. 12 shows the results of the simulated temperature with and without wave effects, compared to the observed temperature evolution. From the potential density evolution (not shown), the temporal variability of MLD is calculated for the upper 10 m (Fig. 11a). The temporal variability of the heat content of the upper 50 m is determined by using temperature and salinity profiles

$$H(t)=\int_{H_1}^{0}[T(z,t)-T_{ref}(t)]\rho(z,t)c_p(z,t)\,dz, \tag{21}$$

where T_{ref},c_p and ρ are reference temperature, specific heat and potential density, respectively, and $H_1=-50$ m. Response of the ocean to the surface heating from early spring to early of autumn is shown in Fig. 12a. The oceanic response has been captured by the model simulations both with and without waves. In the absence of wave effects, for the period starting in the early autumn, the simulation predicts a weaker deepening of the mixed layer and a warmer sea surface temperature, on average, about 3 °C warmer than the observations. Including the wave effects, the modelled temperature is in better agreement with the observations. Fig. 11 shows that the times with deeper

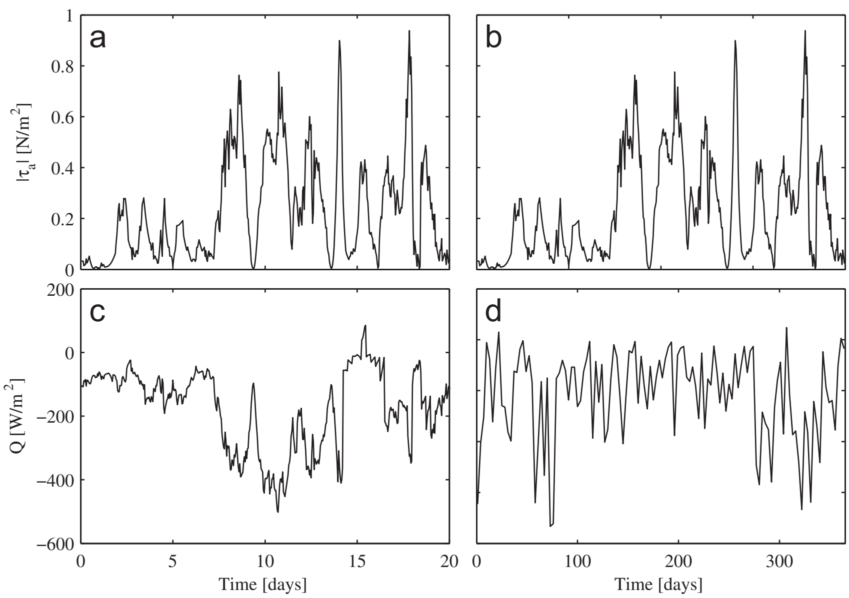

Fig. 9. Wind stresses and net heat fluxes for (a and c) the northern North Sea in 7–27 October 1966, (b and d) OWS Papa for the whole year 1966.

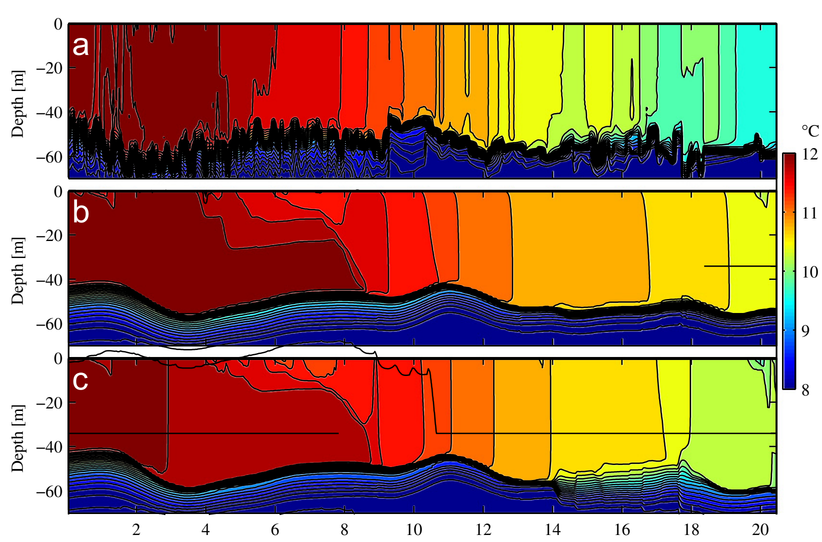

Fig. 10. Depth-time evolution in the period between 7 and 27 October 1966 in the northern North Sea of (a) the observed temperature, (b) the modelled temperature without wave effects, and (c) the simulation result using wave forcing.

(shallower) MLD (Fig. 11a) correspond to times of increased (decreased) ocean heat content, except for a period in winter 1966 (Fig. 11b). It can be seen that including wave forcing gives a better agreement with and smaller deviation from observations in comparison with the no-wave case.

Fig. 13 shows the influence of wave forcing on the vertical profiles of temperature in more detail. The profiles are 12 h averaged in time, centered at days marked in Fig. 12 including early spring when there is positive heat flux from the atmosphere to the ocean (Fig. 13a), the spring–summer when ocean gains heat and winds are relatively weak, early-autumn period (Fig. 13b and c), and for the middle autumn (Fig. 13d).

4. Summary and concluding remarks

The impact of wind-induced gravity waves on the surface Ekman currents and on the upper ocean mixing has been studied using two one-dimensional numerical models: a simple steady state numerical technique (GFEM) and a modification of the

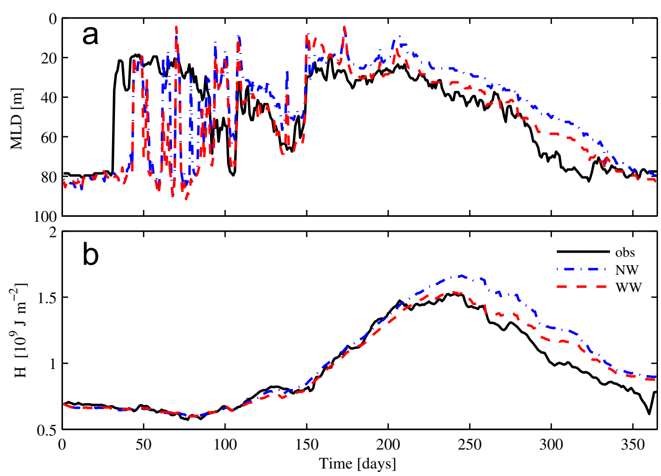

Fig. 11. Temporal variability of (a) MLD and (b) heat content of the upper 50 m in OWS Papa in the northern Pacific Ocean for the entire duration of the experiment in 1966.

turbulent closure model GOTM. The theoretical basis presented by Jenkins (1986, 1987, 1989) was applied for modification of momentum and energy equations by including the wave-induced stress, wind energy input, wave dissipation, and Stokes drift. To calculate these wave induced parameters, the DP wave energy spectrum was employed to approximate a fully developed wind generated sea for a sufficiently large fetch.

A classical continuous Galerkin finite element method as an accurate numerical technique was applied to solve the wave modified Ekman current governing differential equations. This technique can be used successfully for a wide range of eddy viscosities in which there is no sharp variation in the vertical shape of eddy viscosity (because it has difficulties capturing steep gradients). Numerical results were compared with the classical Ekman solution and previously published observations. In agreement with earlier studies, the results showed that: the Stokes drift is the most important factor of wave forcing and it affects both the surface current magnitude (by more than 35%) and the angular turning (by more than 30%) in comparison with the classical Ekman solution; the upper ocean dynamics in the presence of wave forcing is sensitive to parameterizations of the wind energy input source term S_{in} and the wave dissipation term, S_{ds}; using the steady state model confines the wave induced momentum near the surface.

To validate the performance of the wave-modified GOTM, a series of experiments were conducted to cover a number of features of upper ocean boundary layer on diurnal and seasonal time scales. Results showed that the dissipation rate of TKE is enhanced in the wavy ocean boundary layer relative to a rigid boundary layer with similar wind stress and heat flux. In idealized model experiment for wave height of about 1.6 m, we applied the scaling of Terray et al. (1996) which relates ϵ to the energy input from the wind to wave to compare modelled ϵ in the presence of wave forcing with previously published observations. The dissipation rate followed Terray et al. (1996) scaling. Two cases of observations (LOTUS3 and EBC) were simulated to study the surface Ekman current with and without wave forcing. Results from the simulations with wave forcing showed better agreement with the observations. Sources of errors in the model results can be attributed to the absence of advection, uncertainty in net surface heat flux calculation, idealized sea state assumption, uncertainties in wave source term parameterizations, choice of

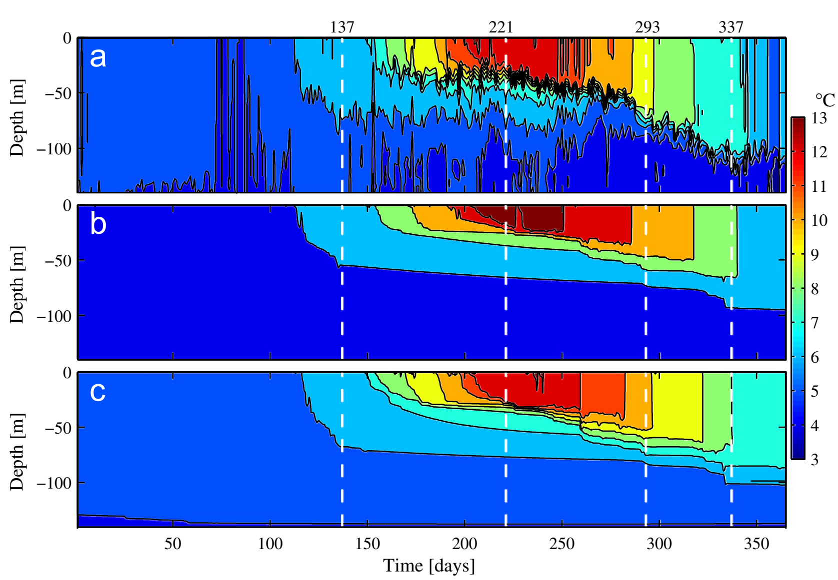

Fig. 12. (a) Temperature evolution at OWS Papa in the northern Pacific Ocean for year 1966, (b) results of GOTM run without wave forcing effects, (c) results of modified GOTM with wave forcing with an ideal sea state parameterization based on the two dimensional DP wave spectrum. Vertical dashed lines mark the days indicated at top for which mean temperature profiles are shown in Fig. 13.

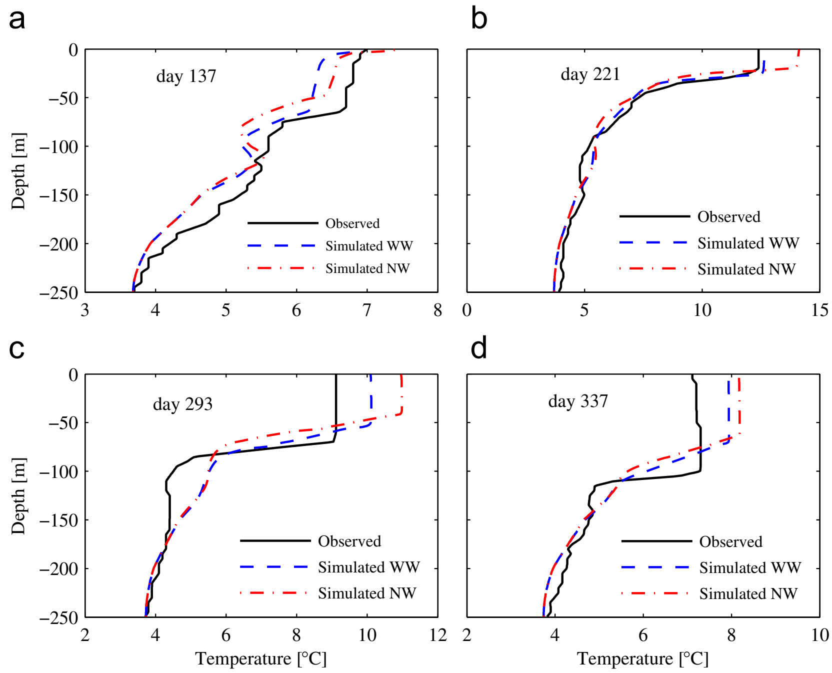

Fig. 13. Measured and simulated temperature profiles at station OWS Papa during year 1966. The simulations were carried out for two cases with wave (WW) and no wave (NW) forcing for different periods of length 12 h centered on days (a) 137, (b) 221, (c) 293, and (d) 337.

the significant wave height parameterization which can affect the comparison with the observations through the scaling, the surface eddy viscosity, measurement errors in hydrography and current meters attached to surfaces floats, bottom friction, sea surface roughness parameterization, and sensitivity of model simulations to the energy and momentum boundary condition parameterizations when breaking waves are included. The modified model performance was further tested by simulating two cases including observations from the northern North Sea and observations covering the annual cycle of the upper ocean layer temperature at OWS Papa in northern Pacific. The modelled results showed that the inclusion of the wave forcing better captures the observed evolution of the upper layer temperature and MLD compared to the no-wave case.

This investigation presented the coupling methodology in terms of required theories, modifications, and parameterizations in order to incorporate the influence of surface wave forcing into an ocean dynamic model. However, wave parameterizations and their implementation in numerical models merit further studies. State of the art observations of turbulence and background parameters in the surface boundary layer are needed to evaluate and improve the skill of the coupling methodology.

Acknowledgements

This work has been funded by the Norwegian Centre for Offshore Wind Energy (NORCOWE) under grant of the Research Council of Norway. The authors thank Kai Christensen, Göran Broström, and two anonymous reviewers for commenting on an earlier version of the manuscript.

Appendix A. Calculating S_{in} and S_{ds}

The formulations which we have used for S_{in} and S_{ds} are as follows: wave growth due to wind forcing is described by

$$S_{in}(f,\theta)=\beta E(f,\theta), \tag{A.1}$$

where the wave energy spectrum $E(f,\theta)$ for the frequency range $[f_{min},f_{max}]$ is determined by the Donelan–Pierson wave energy spectrum (Appendix D), and the spectrum for frequencies $f>f_{max}$ is assumed to be proportional to f^{-5}. From Hasselmann et al. (1988)

$$\beta=\max[0,0.25\varepsilon(28x-1)]\omega, \tag{A.2}$$

and from Janssen (1991), we may write

$$\beta=\omega\varepsilon\beta_w x^2, \tag{A.3}$$

where $\varepsilon=\rho_a/\rho_w=1.25\times10^{-3}$, $x=\max[0,(u_*^a/c)\cos(\theta-\phi)]$, u_*^a is the air-side friction velocity (defined in Eq. (A.8) below), $\omega=2\pi f$ is the angular frequency, $c=\omega/k$ is the phase velocity, θ is the wave direction, ϕ is the wind direction, and β_w is the Miles parameter which can be written as

$$\beta_w=\frac{1.2}{\kappa^2}\mu\ln^4\mu,\quad \mu\le 1, \tag{A.4}$$

where the dimensionless critical height μ is given by

$$\mu=\frac{gz_e}{c^2}\exp(\kappa/x),$$

with g being the gravitational acceleration and $\kappa=0.41$ the von Kármán constant. The effective roughness length z_e is expressed as

$$z_e=\frac{z_0}{\sqrt{1-\frac{\tau_{wave}}{\tau_{tot}}}}, \tag{A.5}$$

where $z_0=\alpha[u_*^a]^2/g$ is the roughness length, $\alpha=0.009$ is Charnock's constant, τ_{tot} and τ_{wave} are the total wind stress and the wave stress, respectively. Furthermore, Janssen (1991) assumed that the wind speed profile is given by

$$U_{10}(z)=\frac{u_*^a}{\kappa}\ln\left(\frac{z+z_e-z_0}{z_e}\right). \tag{A.6}$$

The dissipation source term S_{ds} due to whitecapping is parameterized based on Hasselmann (1974)

$$S_{ds}(f,\theta)=-2.25\overline{\omega}(E_{tot}\overline{k}^2)^2\left(\frac{k}{\overline{k}}+\frac{k^2}{\overline{k}^2}\right)E(f,\theta), \tag{A.7}$$

where $\overline{\varpi}$ is the mean angular frequency, $\overline{k}$ is the mean wavenumber, and E_{tot} is the energy density. In above expressions, the friction velocities for the air-side, u_*^a, and the water-side, u_*^w, are given by

$$u_*^a = \sqrt{\tau_{tot}/\rho_a}; \quad u_*^w = \sqrt{\tau_{tot}/\rho_w}, \tag{A.8}$$

where $\tau_{tot} = \rho_a C_D U_{10}^2$ is the total surface stress, and C_D is a drag coefficient that we assume to be linearly dependent on the wind speed for large wind speed and independent of wind speed below the value of 7.5 m s^{-1} that is given from Wu (1982) as

$$C_D(U_{10}) = \begin{cases} 1.2875 \times 10^{-3}, & U_{10} < 7.5 \text{ m s}^{-1}, \\ (0.8+0.065U_{10}) \times 10^{-3}, & U_{10} \geq 7.5 \text{ m s}^{-1}. \end{cases} \tag{A.9}$$

Ignoring the directional characteristic of $S_{ds}(f,\theta)$ and $S_{in}(f,\theta)$, the frequency dependent representations of them are given as

$$S_{in}(f) = \int_\theta S_{in}(f,\theta)\, d\theta \quad \text{and} \quad S_{ds}(f) = \int_\theta S_{ds}(f,\theta)\, d\theta. \tag{A.10}$$

Appendix B. Iterative algorithm for calculating τ^J_{wave} and τ_{tot}

The wave stress based on the exponential growth rate introduced in Eq. (A.3) is prescribed iteratively using the following calculation scheme. Obtain U_{10}, wind direction, wave direction, frequency vector, wave energy spectrum, and number of realizations as input data

1. update u_*^a, z_0, $r = \tau_{wave}/\tau_{tot}$ and z_e for given wind and wave-induced stress;
2. perform the wave stress calculation using Eq. (3): for convenience, the wave stress defined in Eq. (3) can be separated into two parts:

   $\overrightarrow{\tau}_{wave} = \tau^L_{wave} + \tau^H_{wave}$,

   where the first and the second terms on the right-hand-side refer to integration of Eq. (3) for intervals $[f_{min}, f_{max}]$ and $[f_{max}, f_\infty]$, respectively. Because the wave spectrum is not represented by the wave model for $f > f_{max}$, the spectrum for this frequency range is assumed to be proportional to f^{-5} (Section 2). Therefore, the wave-induced stress for the full frequency range is calculated as follows:
   - calculate $S_{in}(f)$ corresponding to the frequency range $[f_{min}, f_{max}]$ using exponential growth rate equation (A.3);
   - calculate $S_{in}(f)$ for the frequency range $[f_{max}, f_\infty]$ in which the wave energy spectrum is approximated by $E(f) = (f/f_{max})^{-5} E(f_{max})$;
   - determine the critical frequency f_c subject to $\Lambda^1_{in}(f_c) < \tau^b_{wave}$ and calculate the correction function $L(X)$ in which $X = 1 + (\tau^b_{wave} - \tau'_{wave})/\Lambda^2_{in}(f_c)$, $\tau'_{wave} = \Lambda^1_{in}(f_c) + \Lambda^2_{in}(f_c)$ and

     $L(X) = X \exp\left(\dfrac{f_i(f_c - f)}{f(f_c - f_i)}\right)$,

     where f_i is the frequency between f_c and f_∞ (Tsagareli et al., 2010);
   - calculate τ^H_{wave} and τ^L_{wave} using Eq. (3) corresponding to the corrected wind input term $S^{corr}_{in}(f) = L(X) S_{in}(f)$ and update the wave-induced stress τ_{wave};
3. calculate τ_{tot} using Eq. (A.8) and update r;
4. reassign variables τ_{tot} using Eq. (A.6) based on the Newton–Raphson iterative technique as

   $\tau^{n+1}_{tot} = \tau^n_{tot} - \dfrac{G(\tau^n_{tot})}{\dot{G}(\tau^n_{tot})}$,

   where "$\cdot$" denotes the derivative with respect to τ and $G(\tau)$ is given as

   $G(\tau) = \kappa U_{10} - \sqrt{\dfrac{\tau}{\rho_a}} \log\left(\sqrt{1-r}\left[\dfrac{\rho_a g z_{ref}}{\alpha \tau} - 1\right] + 1\right)$,

   in which z_{ref} is the reference height (here 10 m), $\alpha = 0.009$ is Charnock's constant and n denotes the number of iteration. To stop the iterative process, one of the following criteria must be fulfilled: $n \leq 100$ or $|\tau^{n+1}_{tot} - \tau^n_{tot}| < 10^{-8}$;
5. repeat from step 1 for the given number of realizations;
6. stop.

In calculating the wave-induced stress, the upper limit of the integral in above algorithm, f_∞, is determining to contribute short wave scales to the total wave stress. The higher f_∞, the more accurate estimation of τ_{wave}. To include shortest waves in the capillary wave range, in this paper f_∞ is set to 10 Hz. Furthermore, the frequency domain $[f_{min}, f_{max}]$ is defined by the interval [0.05,0.5].

Appendix C. Galerkin finite element method (GFEM)

The GFEM is a member of weighted residual techniques that the approximate solution for $\mathbf{U}$ is written directly in terms of nodal unknowns based on a set of low-order piecewise polynomials. In this method, first, the approximate domain $\Omega = [z_{bot}, z_{surf}]$ is divided into N_z elements at nodes $z_{bot} = z_0 < z_1 < \cdots < z_{N_z} = z_{surf}$. The corresponding weak form of the governing partial differential equation (Eq. (19)) is constructed on each local element. The weak form is the point of departure for the finite element discretization. We define the linear space of all weight (test) functions, w_n, by $H^1_0(\Omega)$ which is the Sobolev space of functions which consists all square-integrable functions having the weak derivatives (Ziemer, 1999). The weak form is determined by integrating Eq. (19) against weight function w_n over each local element $\Omega_m = [z_{m-1}, z_m]$ which gives

$$\int_{\Omega_m} \frac{\partial}{\partial z}\left(\nu^e_t \frac{\partial \mathbf{U}^e}{\partial z}\right) w_n\, dz = \int_{\Omega_m} [i f_{cor}(\mathbf{U}^e + \mathbf{U}^e_s) + \mathbf{F}_{ds}] w_n\, dz. \tag{C.1}$$

The first integral in Eq. (C.1) is rewritten, by applying integration by parts

$$-\int_{\Omega_m} \nu^e_t \frac{\partial \mathbf{U}^e}{\partial z} \frac{\partial w_n}{\partial z}\, dz + \left[\nu^e_t \frac{\partial \mathbf{U}^e}{\partial z} w_n\right]_{\Omega_m}, \tag{C.2}$$

where second term determines boundary condition at end nodes of element Ω_m. The third stage in the finite element method (FEM) is the construction of an approximate solution which $\mathbf{U}$ is expanded as a set of shape functions. These shape functions in the Galerkin method are chosen from the same family as the weight functions. In this study the shape functions are assumed to be linear one-dimensional functions $\phi_m(z)$, $m = 1, 2$ that are non-zero only within $\Omega_{m-1} \bigcup \Omega_m$

$$\phi_m(z) = \begin{cases} \dfrac{z - z_{m-1}}{z_m - z_{m-1}}, & z \in \Omega_{m-1}, \\ \dfrac{z_{m+1} - z}{z_{m+1} - z_m}, & z \in \Omega_m, \\ 0 & \text{otherwise}. \end{cases} \tag{C.3}$$

Thus the approximate solution on each element is defined as

$$\mathbf{U}^e(z) = \sum_{n=1}^{2} \tilde{u}^e_n \phi_n(z). \tag{C.4}$$

It must be noted that these shape functions can be expressed conventionally in an element-based local coordinate system by mapping the interval Ω_m into [0, 1] as follows:

$\phi_1(\xi) = 0.5(1+\xi), \quad \phi_2(\xi) = 0.5(1-\xi), \quad \xi \in [0, 1].$

Table 2
Error estimations of GFEM for different depths.

Depth (m)	5	10	15	20	25	30	35	40
$\lvert U_{nw}-U_E\rvert/10^{-5}$	3.574	3.353	3.003	2.596	2.186	1.804	1.465	1.175
$\lvert U_{ww}-U_{ME}\rvert/10^{-4}$	6.336	6.145	4.983	3.779	2.778	2.009	1.436	1.023

Thus, the integrations in Eq. (C.4) are performed over the domain [0,1].

By substituting Eq. (C.4) into Eq. (C.1) and taking $w_n = \phi_n(z)$, the following discrete form is obtained on each element Ω_m:

$$\sum_{m=1}^{2}\left[-\int_{\Omega_m} \nu_t^e \frac{\partial \phi_m}{\partial z}\frac{\partial \phi_n}{\partial z}\,dz - if_{cor}\int_{\Omega_m}\phi_m\phi_n\,dz\right]\tilde{u}_m^e = \int_{\Omega_m}[if_{cor}\mathbf{U}_s + \mathbf{F}_{ds}]\phi_n\,dz - \Gamma^e,$$

where Γ^e is the second term in Eq. (C.2) and $n=1,2$. Assembling and applying upper and lower boundary conditions lead to the following system of

$$A\tilde{U}_E = B, \tag{C.5}$$

where due to Eq. (C.3), A is a tridiagonal matrix and B is a vector. To check the accuracy of this numerical technique, the differences between the classical Ekman solution and GFEM are shown in Table 2. These comparisons are made by $f_{cor} = 1.2\times10^{-4}$ and $U_{10}=10\ \mathrm{m\,s^{-1}}$. U_{nw} and U_{ww} show the numerical solutions without and with wave forcing, respectively. Meanwhile, U_E and U_{ME} are the classical and wave modified Ekman current solutions (Appendix E). The error values obtained show that the GFEM is sufficiently accurate for many modelling purposes in which the eddy viscosity is assumed to be a smooth function of depth.

Appendix D. The Donelan–Pierson wave spectrum

In this study, the two dimensional wavenumber Donelan and Pierson spectrum (Donelan and Pierson, 1987) is applied for the modelling of a fully developed wind generated sea

$$E(k,\theta) = \exp\left(-\frac{g^2}{k^2(1.2U_{10})^4}\right)1.7^{\Gamma}\Omega, \tag{D.1}$$

where

$$\Omega = \frac{0.00162U_{10}}{k^{2.5}g^{0.5}}\mu\left(\frac{k}{k_p}\right)\cosh^{-2}\left[\mu\left(\frac{k}{k_p}\right)\theta\right] \quad (0<k<\infty,\ -\pi<\theta<\pi),$$

and $\Gamma = \exp\{-1.22[1.2U_{10}k^{0.5}/g^{0.5}-1]^2\}$, θ is the wave direction relative to the wind, k and k_p are the wavenumber and wavenumber at the spectral peak, respectively, $k_p = g/(1.2U_{10})^2$, U_{10} is the wind speed at the reference height 10 m, g is the acceleration due to gravity and μ is given by

$$\mu(x) = \begin{cases} 1.24, & x\in[0,0.31),\\ 2.61x^{0.65}, & x\in[0.31,0.9),\\ 2.28x^{-0.65}, & x\in[0.9,10). \end{cases}$$

Non-directional wave energy spectrum is defined as

$$E(k) = \int_\theta E(k,\theta)\,d\theta. \tag{D.2}$$

Appendix E. Exact solution of Ekman current for constant eddy viscosity in the presence of wave forcing

Assume the eddy viscosity ν is independent of depth. Substituting ν into Eq. (19) leads to an inhomogeneous second order linear differential equation. Eq. (19) can be rewritten in the following general form:

$$\frac{\partial^2\mathbf{U}}{\partial z^2} + p(z)\mathbf{U} = Q(z), \tag{E.1}$$

where $P(z)$ and $Q(z)$ are the depth dependent functions. The solution of this nonhomogeneous equation can be written in the form

$$\mathbf{U}(z) = \mathbf{U}_g(z) + \mathbf{U}_p(z), \tag{E.2}$$

where $\mathbf{U}_g(z) = A\mathbf{U}_1(z) + B\mathbf{U}_2(z)$ is a homogeneous solution where $\mathbf{U}_1$ and $\mathbf{U}_2$ are linearly independent, and $\mathbf{U}_p(z)$ is a particular solution of the nonhomogeneous second order Eq. (E.1) which can be calculated as (Boyce and DiPrima, 2001)

$$\mathbf{U}_p(z) = -\mathbf{U}_1(z)\int_{-\infty}^{z}\frac{\mathbf{U}_2(z')Q(z')}{W[\mathbf{U}_1,\mathbf{U}_2](z')}\,dz' + \mathbf{U}_2(z)\int_{-\infty}^{z}\frac{\mathbf{U}_1(z')Q(z')}{W[\mathbf{U}_1,\mathbf{U}_2](z')}\,dz', \tag{E.3}$$

where $W[x,y](z) = x\,dy/dz - y\,dx/dz$ is the Wronskian of x and y. In this case $\mathbf{U}_1(z) = \exp(jz)$, and $\mathbf{U}_2(z) = \exp(-jz)$, where $j = (1+\sqrt{-1}\,\mathrm{sign}(f_{cor}))/h_e$, $h_e = \sqrt{2\nu/|f_{cor}|}$ is the depth of the Ekman layer, sign($\cdot$) is the sign function, and $W[\mathbf{U}_1,\mathbf{U}_2](z) = -2j$. The particular solution is given by

$$\mathbf{U}_p(z) = \frac{1}{j\nu}\int_{-\infty}^{z}[if_{cor}\mathbf{U}_s + \mathbf{F}_{ds}](z')\sinh(z-z')\,dz'. \tag{E.4}$$

By satisfying the bottom boundary condition ($\mathbf{U}\to0$ as $z\to-\infty$) and surface (Eq. (11)), the unknown parameters A and B in the expression of $\mathbf{U}_g(z)$ are determined such that $B=0$ and

$$A = \frac{\overrightarrow{\tau}^{surf}_{mod}}{j\rho_w\nu} - \frac{1}{j\nu}\int_{-\infty}^{0}[if_{cor}\mathbf{U}_s + \mathbf{F}_{ds}](z')\cosh(z')\,dz'.$$

References

Andrews, D., McIntyre, M., 1978. An exact theory of nonlinear waves on a Lagrangian mean flow. Journal of Fluid Mechanics 89, 609–646.

Anis, A., Moum, J.N., 1995. Surface wave–turbulence interactions. Scaling $\epsilon(z)$ near the sea surface. Journal of Physical Oceanography 25, 2025–2045.

Ardhuin, F., Jenkins, A.D., 2006. On the interaction of surface wave and upper ocean turbulence. Journal of Physical Oceanography 36, 551–557.

Babanin, A.V., Haus, B.K., 2009. On the existence of water turbulence induced by nonbreaking surface waves. Journal of Physical Oceanography 39, 2675–2679.

Boyce, W., DiPrima, R.C., 2001. Elementary Differential Equations and Boundary Value Problems. John Wiley and Sons, Inc.

Burchard, H., Baumert, H., 1995. On the performance of a mixed-layer model based on the $k-\epsilon$ turbulence closure. Journal of Geophysical Research 100, 8523–8540.

Burchard, H., Bolding, K., 2001. Comparative analysis of four second moment turbulence closure models for the oceanic mixed layer. Journal of Physical Oceanography 31, 1943–1968.

Craig, P.D., 1996. Velocity profiles and surface roughness under breaking waves. Journal of Geophysical Research 101 (C1), 1265–1277.

Craig, P.D., Banner, M.L., 1994. Modeling wave-enhanced turbulence in the ocean surface layer. Journal of Physical Oceanography 24, 2546–2559.

Dai, D., Qiao, F., Sulisz, W., Han, L., Babanin, A.V., 2010. Notes and correspondence: an experiment on the nonbreaking surface-wave-induced vertical mixing. Journal of Physical Oceanography 40, 2180–2188.

Donelan, M.A., Pierson, W.J.P., 1987. Radar scattering and equilibrium ranges in wind-generated waves with application to scatterometry. Journal of Geophysical Research 92, 4971–5029.

Drennan, W.M., Donelan, M.A., Terray, E.A., Katsaros, K.B., 1996. Oceanic turbulence dissipation measurements in SWADE. Journal of Physical Oceanography 26, 808–815.

Feddersen, F., Trowbridge, J.H., 2005. The effect of wave breaking on surf-zone turbulence and alongshore currents: a modeling study. Journal of Physical Oceanography 35, 2187–2203.

Gemmrich, J., 2010. Strong turbulence in the wave crest region. Journal of Physical Oceanography 40, 583–595.

Gemmrich, J.R., Farmer, D.M., 2004. Near-surface turbulence in the presence of breaking waves. Journal of Physical Oceanography 34, 1068–1086.
Gerbi, G.P., Trowbridge, J.H., Terray, E.A., Plueddemann, A.J., Kukulka, T., 2009. Observations of turbulence in the ocean surface boundary layer: energetics and transport. Journal of Physical Oceanography 39, 1077–1096.
Guan, C.L., Xie, L., 2004. On the linear parameterization of drag coefficient over sea surface. Journal of Physical Oceanography 32, 2847–2851.
Hasselmann, K., 1974. On the spectral dissipation of ocean waves due to white-capping. Boundary-Layer Meteorology 6, 107–127.
Hasselmann, S., Hasselmann, K., Komen, G.K., Janssen, P., Ewing, J.A., Cardone, V., 1988. The WAM model: a third generation ocean wave prediction model. Journal of Physical Oceanography 18, 1775–1810.
Hasselmann, K., 1970. Wave-driven inertial oscillations. Geophysical Fluid Dynamics 1, 463–502.
He, H., Chen, D., 2011. Effects of surface wave breaking on the oceanic boundary layer. Geophysical Research Letters 38. doi:10.1029/2011GL046665.
Huang, C.J., Qiao, F., Song, Z., Ezer, T., 2011. Improving simulation of the upper ocean by inclusion of surface waves in the Mellor–Yamada turbulence scheme. Journal of Geophysical Research 116, C01007. doi:10.1029/2010JC006320.
Huang, N.E., 1971. Derivation of Stokes drift for a deep-water random gravity wave field. Deep-Sea Research 18, 255–259.
Janssen, P.A.E.M., 1989. Wave-induced stress and the drag of air flow over sea waves. Journal of Physical Oceanography 19, 745–753.
Janssen, P.A.E.M., 1991. Quasi-linear theory of wind-wave generation applied to wave forecasting. Journal of Physical Oceanography 21, 1631–1642.
Jeffreys, H., 1925. On the formation of waves by wind. Proceedings of the Royal Society A 110, 341–347.
Jenkins, A.D., 1986. A theory for steady and variable wind and wave induced currents. Journal of Physical Oceanography 16, 1370–1377.
Jenkins, A.D., 1987. Wind and wave induced currents in a rotating sea with depth-varying eddy viscosity. Journal of Physical Oceanography 17, 938–951.
Jenkins, A.D., 1989. The use of a wave prediction model for driving a near-surface current model. Deutsche Hydrographische Zeitschrift 42, 133–149.
Jenkins, A.D., 1992. A quasi-linear eddy-viscosity model for the flux of energy and momentum to wind waves, using conservation-law equations in a curvilinear coordinate system. Journal of Physical Oceanography 22 (8), 843–858.
Jones, I.S.F., Toba, Y., 2008. Wind Stress Over the Ocean. Cambridge University Press.
Jones, N.L., Monismith, S.G., 2007. The influence of whitecapping waves on the vertical structure of turbulence in a shallow estuarine embayment. Journal of Physical Oceanography 38, 1563–1580.
Kantha, L.H., Clayson, C.A., 2004. On the effect of surface gravity waves on mixing in the oceanic mixed layer. Ocean Modelling 6, 101–124.
Kitaigorodskii, S.A., Donelan, M.A., Lumley, J.L., Terray, E.A., 1983. Wave–turbulence interactions in the upper ocean. Part II. Statistical characteristics of wave and turbulent components of the random velocity field in the marine surface layer. Journal of Physical Oceanography 13, 1988–1999.
Komen, G.J., Hasselmann, S., Hasselmann, K., 1984. On the existence of a fully developed wind–sea spectrum. Journal of Physical Oceanography 14, 1271–1285.
Kudryavtsev, V.N., Makin, V.K., 2002. Coupled dynamics of short waves and the airflow over long surface waves. Journal of Geophysical Research 107 (C12).
Lewis, D.M., Belcher, S.E., 2004. Time-dependent coupled Ekman boundary layer solutions incorporating Stokes drift. Dynamics of Atmospheres and Oceans 37, 313–351.
Longuet-Higgins, M.S., 1953. Mass transport in water waves. Philosophical Transactions of the Royal Society, Series A 245, 535–581.
Mastenbroek, C., Burgers, G.J.H., Janssen, P.A.E.M., 1993. The dynamical coupling of a wave model and a storm surge model through the atmospheric boundary layer. Journal of Physical Oceanography 23, 1856–1866.
McWilliams, J.C., 1996. Modeling the oceanic general circulation. Annu. Rev. Fluid. Mech. 28, 215–248.
McWilliams, J., Restrepo, J., 1999. The wave driven ocean circulation. Journal of Physical Oceanography 29, 2523–2540.
Mellor, G.L., Blumberg, A.F., 2004. Wave breaking and ocean surface layer thermal response. Journal of Physical Oceanography 34, 693–698.
Mellor, G.L., Yamada, T., 1982. Development of a turbulence closure model for geophysical fluid problems. Reviews of Geophysics and Space Physics 20, 851–875.
Melville, W.K., 1996. The role of surface-wave breaking in air–sea interaction. Annual Review of Fluid Mechanics 28, 279–321.
Miles, J.W., 1957. On the generation of surface waves by shear flows. Journal of Fluid Mechanics 3, 185–204.
Moon, I.J., 2005. Impact of a coupled ocean wave–tide-circulation system on coastal modeling. Ocean Modelling 8, 203–236.
Perrie, W., Tang, C.L., Hu, Y., DeTracy, B.M., 2003. The impact of waves on surface currents. Journal of Physical Oceanography 33, 2126–2140.
Phillips, O.M., 1958. The equilibrium range in the spectrum of wind-generated waves. Journal of Fluid Mechanics 4, 426–434.
Pollard, R., 1973. Interpretation of near-surface current meter observations. Deep-Sea Research 20, 261–268.
Polton, J.E., Lewis, D.M., Belcher, S.E., 2005. The role of wave-induced Coriolis–Stokes forcing on the wind-driven mixed layer. Journal of Physical Oceanography 35, 444–457.
Price, J.F., Sundermeyer, A., 1999. Stratified Ekman layers. Journal of Geophysical Research 104, 20467–20494.
Qiao, F., Yuan, Y., Yang, Y., Zheng, Q., Xia, C., Ma, J., 2004. Wave-induced mixing in the upper ocean: distribution and application to global ocean circulation model. Geophysical Research Letters 31, L11303. doi:10.1029/2004GL019824.
Rascle, N., Ardhuin, F., Terray, E.A., 2007. Drift and mixing under the ocean surface: a coherent one-dimensional description with application to unstratified conditions. Journal of Geophysical Research 111, C03016. doi:10.1029/2005JC003004.
Resio, D.T., Long, C.E., 2004. Equilibrium-range constant in wind-generated wave spectra. Journal of Geophysical Research 109, 1–14.
Saetra, Ø., Albretsen, J., Janssen, P., 2007. Sea-state-dependent momentum fluxes for ocean modeling. Journal of Physical Oceanography 37, 2714–2725.
Schumann, U., Gerz, T., 1995. Turbulent mixing in stably stratified shear flows. Journal of Applied Meteorology 34, 33–48.
Shaw, W.J., Stanton, T.P., McPhee, M.G., Morison, J.H., Martinson, D.G., 2009. Role of the upper ocean in the energy budget of Arctic sea ice during SHEBA. Journal of Geophysical Research 114. doi:10.1029/2008JC004991.
Snyder, R.L., Elliot, F.W.D.J., Long, R.B., 1981. A field study of wind generation of ocean waves. Journal of Fluid Mechanics 102, 1–59.
Soloviev, A., Lukas, R., 2003. Observation of wave-enhanced turbulence in the near-surface layer of the ocean during TOGA-COARE. Deep-Sea Research I 50, 371–395.
Song, J.B., 2009. The effects of random surface waves on the steady Ekman current solutions. Deep-Sea Research I 56, 659–671.
Song, J.B., Huang, Y.S., 2011. An approximate solution of wave-modified Ekman current for gradually varying eddy viscosity. Deep-Sea Research I 58, 668–676.
Stips, A., Burchard, H., Bolding, K., Prandke, H., Simon, A., Wuest, A., 2005. Measurement and simulation of viscous dissipation in the wave affected surface layer. Deep-Sea Research II 52, 1133–1155.
Sullivan, P.P., McWilliams, J.C., 2010. Dynamics of winds and currents coupled to surface waves. Annual Review of Fluid Mechanics 42, 19–42.
Sullivan, P.P., McWilliams, J.C., Melville, W.K., 2007. Surface gravity wave effects in the oceanic boundary layer: large-eddy simulation with vortex force and stochastic breakers. Journal of Fluid Mechanics 593, 405–452.
Tang, C.L., Perrie, W., Jenkins, A.D., DeTracey, B.M., Hu, Y., Toulany, B., Smith, P.C., 2007. Observation and modeling of surface currents on the Grand Banks: A study of the wave effects on surface currents. Journal of Geophysical Research 112, 1–16.
Terray, E.A., Donelan, M.A., Agrawal, Y.C., Drennan, W.M., Kahma, K.K., Williams, A.J., Hwang, P.A., Kitaigorodski, S.A., 1996. Estimates of kinetic energy dissipation under breaking waves. Journal of Physical Oceanography 26, 792–807.
Tolman, H.L., 2002. User Manual and System Documentation of Wavewatch III Version 2.22. Technical Report NOAA. Silver Spring, MD (available at 〈http://polar.ncep.noaa.gov/waves〉).
Tolman, L.H., Chalikov, D., 1996. Source terms in a third-generation wind wave model. Journal of Physical Oceanography 26, 2497–2518.
Tsagareli, K.N., Babanin, A.V., Walker, D.J., Young, I.R., 2010. Numerical investigation of spectral evolution of wind waves. Part I. Wind-input source function. Journal of Physical Oceanography 40, 656–666.
Wam, G., 1988. The WAM model: a third generation ocean wave prediction model. Journal of Physical Oceanography 18, 1775–1810.
Wang, W., Huang, R.X., 2004. Wind energy input to the surface waves. Journal of Physical Oceanography 34, 1276–1280.
Wanninkhof, R., Asher, W.E., Ho, D.T., Sweeney, C., McGillis, W.R., 2009. Advances in quantifying air–sea gas exchange and environmental forcing. Annual Review of Marine Science 1, 213–244.
Weber, J.E., 1983a. Attenuated wave-induced drift in a viscous rotating ocean. Journal of Fluid Mechanics 137, 115–129.
Weber, J.E., 1983b. Steady wind and wave induced currents in the open ocean. Journal of Physical Oceanography 13, 524–530.
Wu, J., 1982. Wind-stress coefficients over sea surface from breeze to hurricane. Journal of Geophysical Research 87 (C12), 9704–9706.
Ziemer, W.P., 1999. Weakly Differentiable Functions. Springer-Verlag, New York.